

Biomechanics of hair fibre growth: a multi-scale modeling approach

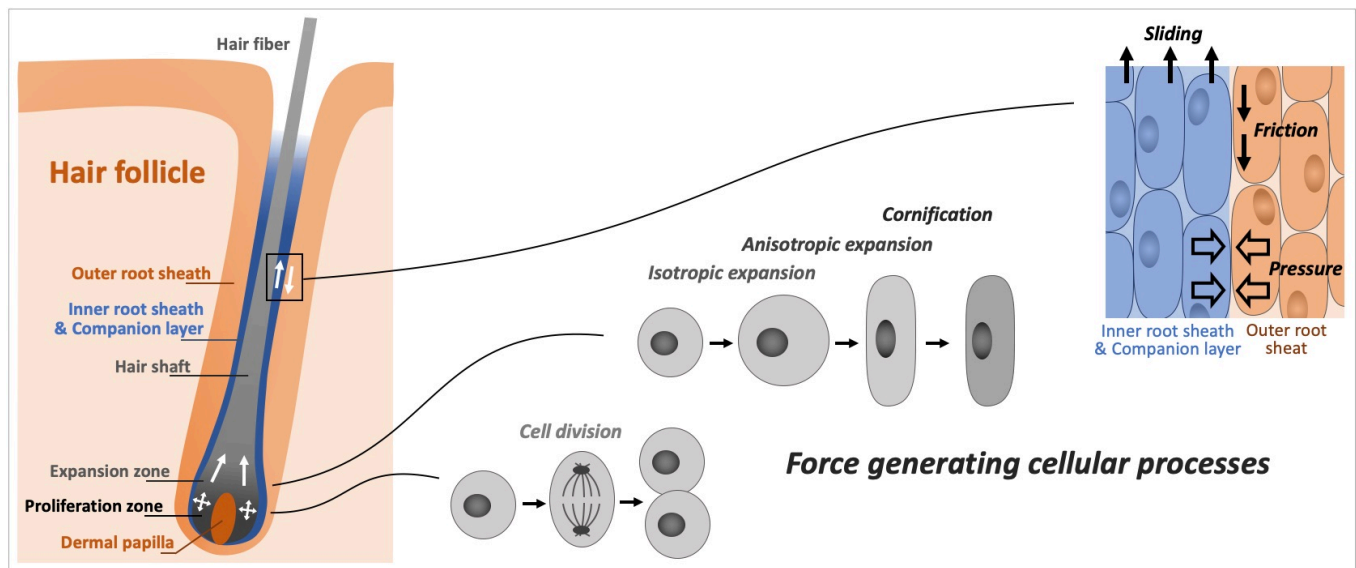
M. Shafayet Zamil¹, Duane P. Harland², Brian K. Fisher³, Michael G. Davis³, James R. Schwartz³, Anja Geitmann^{1*}

¹Department of Plant Science, McGill University, Macdonald Campus, 21111 Lakeshore, Ste-Anne-de-Bellevue, Québec H9X 3V9, Canada

²Food and Biobased Products Group, AgResearch Ltd, Private Bag 4749, Christchurch 8140, New Zealand

³Procter & Gamble Beauty Care, 8700 Mason Montgomery Road Mason, OH 45040-9462 USA

*Corresponding Author: Anja Geitmann (geitmann.aes@mcgill.ca), www.geitmannlab.org



Abstract

In an actively growing scalp hair, the cells proliferating at the basal zone of the hair follicle commence a journey of approximately 4 mm in two weeks before emerging from the scalp surface as a strong rigid fiber. This maturation process of the nascent hair fiber involves many biological, biochemical and biomechanical factors. While we have a rich understanding of the regulatory elements governing biological and biochemical processes, our understanding of the role of biomechanical factors in hair fiber protrusion is virtually null. By adopting a multiscale mechanical modeling approach, here we sought to add a new dimension to the understanding of hair fiber growth. An overall mechanical model constructed to correspond to the entire follicle is complemented and informed by predictions obtained from tissue and cell-scale models. Combined, the simulations suggest that biomechanical features such as follicle geometry, hydrostatic state of tissues layers, material stiffness, keratinization-mediated hardening, and desmosome-correlated shear sliding behaviors are likely to play important roles in hair fiber protrusion. The simulation results predict fine tuning of biomechanical parameters to be a key strategy to ensure smooth hair fiber protrusion while maintaining sufficient anchoring strength against external disturbance. The *in silico* model of a hair follicle sets a framework for experimental validation and guides the investigation of biomechanical underpinnings of hair growth processes.

Keywords

Mechanical model, finite element analysis, biomechanics, hair follicle, hair growth, computational analysis

1 Introduction

The human scalp produces up to 2 m of new hair fiber per hour, all individual hairs combined (Ebling, 1991; Saitoh, 1969). Hair fiber production occurs within hair follicles, structures with such a distinct and sophisticated coordination of biological activities that they are often characterized as a mini-organs. The hair growth cycle is typically characterized by three sequential phases defining the status of the follicle, namely: a growth phase (anagen), a regression phase (catagen), and a resting phase (telogen). During the growth phase, cells proliferate at the base of the follicle and this proliferation is thought to push up the ascending fiber leading to the protrusion of the hair, or hair growth. Soon after leaving the basal bulb region, the nascent hair traverses approximately 4 mm to emerge from the scalp surface, a process that takes about 2 weeks (Jimenez et al., 2011). The cells of the nascent fiber are alive in the bulb, but soon undergo a programmed cell death which is an integral part of fiber development. Consequently, the hair fiber proper consists of dead material (Jones et al., 2018). During its progress towards the scalp surface, the hair fiber undergoes physical and chemical changes as it matures and keratinizes. Hair fiber production results from a combined process involving biological, biochemical, and biomechanical processes (Lim et al., 2019), and while the former are well characterized, almost nothing is known about the biomechanical underpinnings. Here we have sought to add a dimension to this concept by assessing hair growth from a physical mechanics perspective and identifying potentially critical structural features that affect and regulate fiber protrusion.

The actively hair-producing follicle consists of a complex structure of concentric layers each of which displays a distinct longitudinal gradient of maturation. The longitudinal differentiation process starts with the proliferation of the outer root sheath (ORS)-derived stem cells positioned along the basement membrane at the lower half portion of the dermal papilla (DP). The progeny of these stem cells is initially undifferentiated, the cells divide, grow and move distally along the direction of the hair growth (Yang et al., 2017). During this process they differentiate into seven distinct concentric cell lines (layers). From outside to inward, these layers include the companion layer (CP), three inner root sheath (IRS) layers (Henle's, Huxley's and IRS cuticle), and three hair fiber layers (fiber cuticle, cortex and medulla). The companion layer grows alongside the IRS layers and acts as an interface between the stationary outer root sheath (ORS) and the moving (growing) IRS and fiber layers (Orwin, 1971). The aim of this study is to use computational modelling to connect morphological and biochemical maturation to biophysical properties that may contribute directly to the process of hair growth.

The maturation of the concentric tissue layers involves three principal processes: (1) rigid body movement of the cells, which includes cellular rotation and intercellular sliding within the tube created by the ORS, (2) morphodynamics of the cells as they are pushed upward, and (3) bio-chemical conversion such as keratinization and cornification. The morphodynamics and the biochemistry of hair formation are understood with the help of molecular and proteomic technologies (Harland, 2018; Harland and Plowman, 2018; Plowman et al., 2015; Schneider et al., 2009; Wang et al., 2006), but the biophysical and biomechanical underpinnings of this process are virtually unknown. For example, the cortex of the hair follicle is known to gradually stiffen from the proximal bulb to distal bulb zone as a result of the formation and structuring of the keratin fiber (Bornschlöggl et al., 2016). However, it is unknown whether this gradual stiffening of the hair follicle cell lines also plays role in physically promoting hair fiber protrusion or as part of the cornification process itself (Greenberg and Fudge, 2013).

Hair fiber growth is subject to two pivotal but seemingly opposite requirements, namely: (1) retention of anchoring strength, and (2) facilitation of hair protrusion from the dermis. In other words, the growing layers of the hair follicle and the protruded keratinized fiber need to be anchored/attached within the stationary dermal canal with sufficient mechanical strength to avoid that the hair fiber detaches when pulled. At the same time, the growing layers of the hair follicle must slide against the static layers sufficiently easily to allow hair extrusion. For both functions the CP-ORS interface is likely to play a pivotal role in regulating the mechanodynamics of hair protrusion (Langbein et al., 2002; Lemasters et al., 2017); yet not much is known about the mechanism governing the adhesion at this gliding plane. The CP develops cytoskeletal and cell junction organization (including desmosomes) indicative of a mechanical function (Langbein et al., 2002; Orwin, 1971) and selective elimination of some cell junction proteins in the CP (e.g. desmogleins 1 and 3) causes a loss of anchoring strength at the CP-ORS interface (Hanakawa et al., 2004). Desmosomes are intercellular junctional complexes, important in tissues exposed to mechanical stress such as epithelial and cardiac muscle (Garrod and Chidgey, 2008), and appear to play a role at the CP-ORS shear interface.

In addition to the shear resistance at the moving-static interface, the biophysical and biochemical processes in the hair follicle proper also present possible sources of forces that either promote (assistive) or counteract (resistive) hair protrusion. Conventionally, the cellular proliferation at the basal zone of the hair follicle is recognized to be the primary source of the assistive force that pushes the hair fiber out of the follicle. The isotropic and anisotropic expansive growth of cells in pre-cortex

and elongation zones of the hair follicle is likely to play a similar role (Orwin and Woods, 1982). During the process of hardening, the cells in the cortex and Henle's layers lose cytoplasmic turgor pressure, leading to the presence of differential pressure states within the layers and zones of the follicle (Bornschlögl et al., 2016). The nature of this differential pressure state, whether assistive (promoting growth) or resistive (impeding growth), is not known. Overall, our current understanding of the hair follicle biology helps us identify several potential sources of physical forces and impedances that putatively influence the growth of the hair fiber directly or indirectly (Fig. 1a). However, our understanding of the nature of these forces and impedances and how they

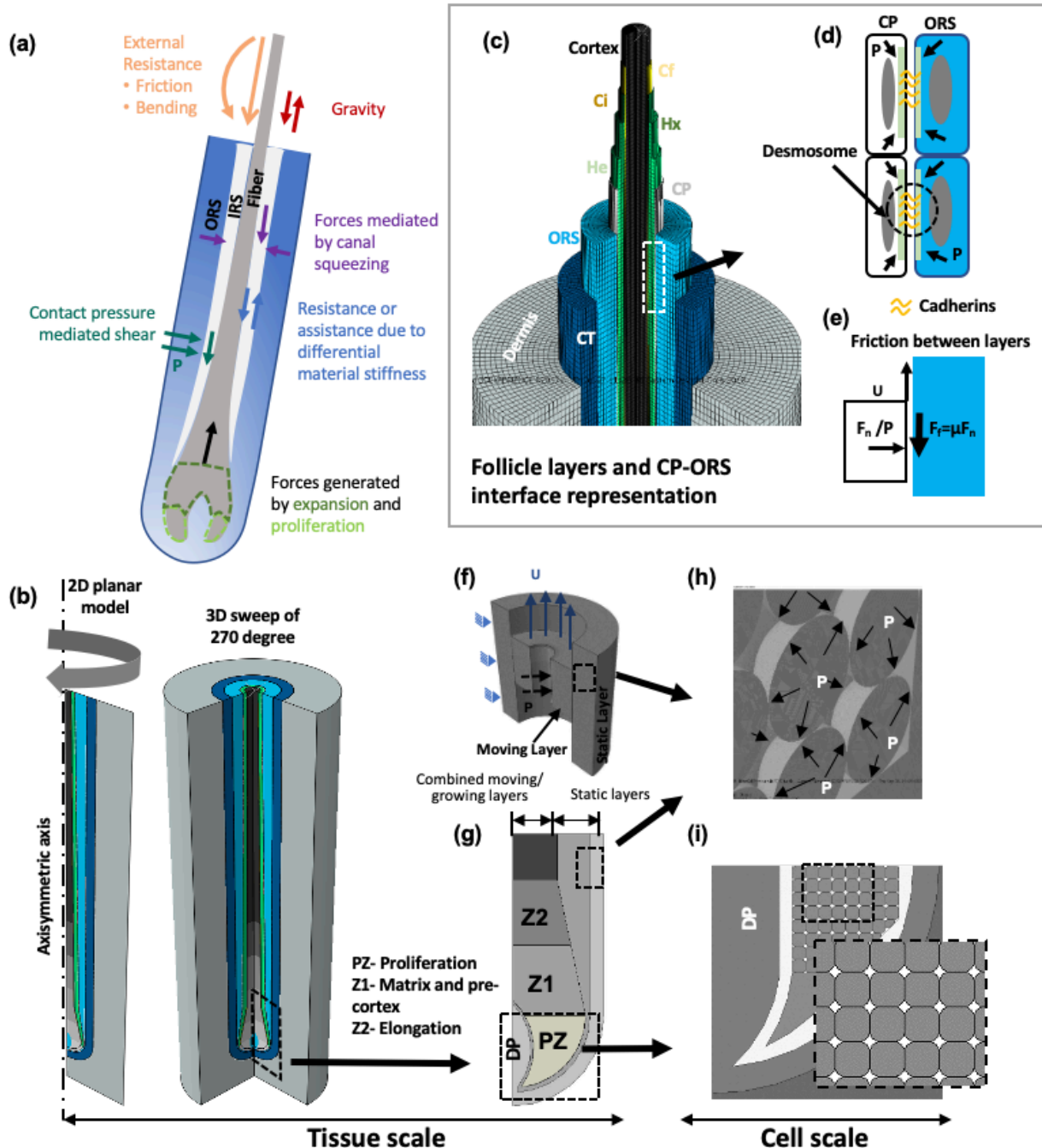


Figure 1. (a) Forces and impedances putatively relevant for hair fiber protrusion during the growth (anagen) phase. (b) Geometry and assembly of whole follicle model. The axisymmetric 2D planar model comprises nine layers, the 360° revolution of which generates a concentric 3D mechanical model. (c) Discretized FEA model showing moving and static layers. Dermis, connective tissue (CT) and outer root sheath (ORS) constitute the static portion of the hair follicle. Companion (CP), three inner root sheath (IRS) layers (Henle's (He), Huxley's (Hx), IRS cuticle (Ci)), and two hair shaft layers (fiber cuticle (Cf), cortex) constitute moving or growing portion of the hair follicle. (d) Detail of the shear interface between moving CP and static ORS layers. (e) Mathematical representation of the frictional behavior between static vs. moving layers. Shear resistance reflects the presence of desmosomes at the CP/ORS interface. (f) Two-body shear-sliding model used to define the underpinnings of the shear resistance between moving and static layers. (g) 2D slice of bulb model encapsulating follicle bulb and suprabulbar zone. (h) 3D cellular scale model translating pressure field to pre-stress field. (i) 2D cellular proliferation model in bulb zone.

influence hair growth is virtually non-existent. The computational modelling approach presented here simulates hair growth as an emergent property integrated from local conditions across the various different cell lines and varied along the developmental process. The framework developed ultimately allows us to predict which structural features and forces critically affect hair growth and which are insignificant in the biomechanical context. The mechanical model allows us to assess the biophysical features that affect the translation of the forces generated by cellular proliferation and expansion in the bulb zone to protrusion of the hair fiber at the scalp surface. In doing so we demonstrate the important role of biomechanics as a mechanism in the growth of mammalian hair.

2 Methods

2.1 Multiscale finite element modeling approach

The model was constructed using finite element analysis (FEA), an engineering methodology developed to computationally simulate the emergent physical behavior of local interactions (e.g., how forces propagate through materials). FEA tools have been used to solve complex engineering problems such as structural, thermal, fluid dynamics and vibrational situations, especially in cases where the analytical solution is impossible to derive (Reddy, 1993). In recent years, FEA-based computational modeling has garnered increasing interest in the biological sciences and has been extensively used to simulate and make predictions for complex biological phenomena related to morphogenesis and structural development (Brodland, 2015, 2004; Dintwa et al., 2011; Fayant et al., 2010; Kam et al., 2012; Pieczywek and Zdunek, 2014; Rayfield, 2007; Sanati Nezhad et al., 2013; Sanati Nezhad and Geitmann, 2013; Stadtländer, 2014; Yi and Puri, 2012). Model development includes identification of the key structures associated with hair growth to a level where location-specific modelling strategies can be created to translate biology and biochemistry into physical realities. This is especially important for interactions at interfaces (e.g., the moving-static CP-ORS interface in the hair follicle).

The structural complexities and the biophysical processes associated with hair fiber protrusion occur across different length scales and key parts of the process have been tied to several different regions of interest (Figs. 1 and 2). Therefore, a multiscale modeling approach was adopted to represent crucial aspects of the process. Five distinct but related FEA models were developed ranging in size and scope from the entire follicle micro-organ to a small cluster of cells simulating cellular growth and intercellular interactions (Fig. 1).

Three of these models were designed to operate at tissue-scale in which individual tissue layers are represented as solid structures (Figs. 1b,f,g). The 'whole follicle model' captures overall follicle anatomy and physiology (Fig. 1b). At this scale, tissue layers are considered as a continuum ignoring the cellular nature. The whole follicle is comprised of a spherical-shaped bulb and a cylindrical-shaped stem (Fig. 2). Within the cylindrical shaft, the geometry (radius and thickness) of the follicle layers remains relatively constant and the biophysical properties change only minimally in longitudinal direction. Within the bulb and proximal bulb zones, both the geometry and material properties of the layers are designed to vary more substantially in longitudinal direction. To assess if the geometry of the bulb zone affects hair fiber protrusion, and if so, which parameters are critical, a second tissue scale model comprising only the bulb and suprabulbar zone was developed (Fig. 1g, 'bulb model'). The bulb model was separately built and eliminated complexity by adopting a single description of material properties for the moving and static layers, respectively. This approach allowed focusing on the geometric factors potentially influencing hair fiber protrusion. The detail of the bulb model will be discussed in the next section. A third tissue scale model was designed to specifically assess the contribution of material properties and boundary conditions to the shear sliding behavior at the interface of moving and static layers (Fig. 1f). This 'shear sliding model' is a simplified two components model comprising one moving and one static layer.

To inform these tissue level models with more detailed geometrical considerations and cell relevant processes, two cell-scale models were developed. The 'pressure to pre-stress model' is designed to estimate average stress induced by hydrostatic cellular pressure in the non-cornified domains of the hair follicle (Fig. 1h). The average stress estimated by this model was then used as a pre-condition in all the simulations performed at tissue and cellular scales. The pre-stressed non-cornified domains not only closely simulate the real follicle but were also a critical condition to generate shear sliding behavior. The details of the shear sliding behavior modeling and rationale are discussed in later sections. The 'cellular proliferation model' simulates cellular proliferation and expansion in the hair follicle bulb and proximal bulb regions (Fig. 1i).

development please refer to Supplemental Material.

The whole follicle model has nine concentric layers revolving around the longitudinal axis (Fig. 1b,c). The dermis, connective tissue (CT) and ORS are non-growing/static layers. In the literature, the CT is also referred to as dermal sheath. Inside the static cylindrical well, the companion layer (CP) and three inner root sheath layers (IRS) envelope three hair shaft layers. Combined, these seven concentric layers form the cluster of growing/moving layers. The IRS layers are from outside to inside: Henle's (He), Huxley's (Hx) and inner root sheath cuticle (Ci) layers. The hair shaft layers comprise fiber cuticle (Cf) and cortex (Cr) layers. Because of its relative thin dimension compared to the whole cortex layer and its location adjacent to the axisymmetric axis, the medulla is not designated by a separate boundary, and is considered as an integral part of the cortex layer for modeling purposes.

The whole follicle axisymmetric geometric model was discretized using CAX4R (4-node bilinear axisymmetric quadrilateral, reduced integration, hourglass control) elements. The solutions of the whole follicle model were carried out for a set of boundary, material and CP-ORS interface conditions pertaining to the study of the hair fiber protrusion.

2.2.2 Bulb model

The bulb model is a separately built model representing a 2D slice of the whole follicle model limited to the bulb (Fig. 1g) proximal of Orwin's threshold (Supplemental Fig. S1). The geometry of the bulb model is in accordance with the corresponding zone of the whole follicle model (Fig. 2) but with simplified layer structure. Instead of defining seven distinct concentric layers, only two layers are used - one layer represents the aggregate of the moving layers and the other represents the aggregate of all static layers. This eliminates the convolution of simulation outcomes by the material properties of the individual layers, and allows focusing on the effect of the shape of the bulb zone. Furthermore, the ORS and CT layers are collectively assigned the material properties designated for ORS.

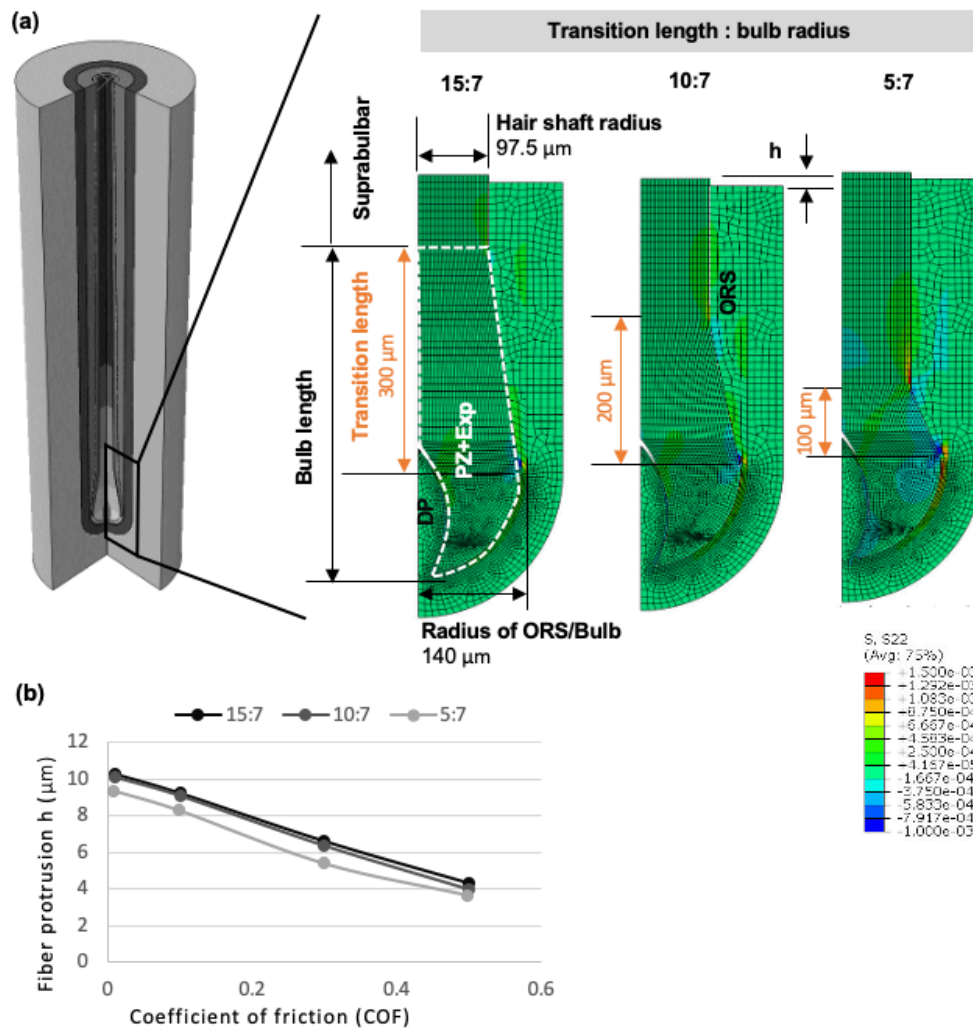


Figure 3. Contribution of bulb shape to hair fiber protrusion. (a) Three versions of the bulb model were developed with varying transition lengths while keeping the bulb size fixed. Based on the aspect ratio of transition lengths and ORS bulb radius, the models were 15:7, 10:7 and 5:7. Simulations were carried out for 6% expansion of PZ and fiber protrusion, h, was measured. (b) Fiber protrusion for three different transition lengths for a range of COF.

Supplemental Material). According to our parametric study: (a) the fiber shaft diameter is smaller than the bulb diameter by a factor of 1.5 ± 0.1 ; (b) the transition length is larger than the bulb diameter by a factor of 2.4 ± 0.4 . Analyzing published microscopic data, the dimensional variability of the transition length to bulb diameter was found to be high (as indicated by a much larger standard deviation). While some of this variability may be due to sample preparation (notably the cutting angle of longitudinal sections), there is likely to be biological variation that critically affects hair fiber protrusion. To be able to probe the effect of this variability, three versions of the bulb model were constructed by varying the transition lengths while keeping the bulb and the shaft diameter fixed (Fig. 3a).

2.2.3 Shear sliding model

To better understand how the stiffness of the layers forming a moving-static interface influences hair protrusion, a simplified two-body axisymmetric FEA model was constructed. The two-body model is composed of two concentric hollow cylindrical shaped components (Fig. 4a). In the model, a $20 \mu\text{m}$ long component (moving layer) slides past a $50 \mu\text{m}$ long static/fixed component. The moving layer is a simplified representation of the ensemble of IRS layers, whereas the static layer represents the ORS, CT and the dermis layers. The axisymmetry ensures that the constructed two-body model resembles the geometry of the hair follicle moving-static interface. To simulate the presence of cell pressure, the moving layer was subjected to 40 Pa pressure, a level of pressure observed in turgid HeLa cells (Fischer-Friedrich et al., 2014), normal to the moving-static layer plane and the static layer was kept fixed at its bottom surface. Simulations were carried out for a $5 \mu\text{m}$ sliding motion of the moving layer for the following scenarios: (1,2) static and moving layers have identical material properties with low stiffness value (500 kPa , 1) and higher stiffness (5000 kPa , 2); (3,4) mismatch in material properties with softer moving layer (500 kPa) and stiffer static layer (5000 kPa) in scenario 3 and the reverse in scenario 4. The lower stiffness value was based on the default

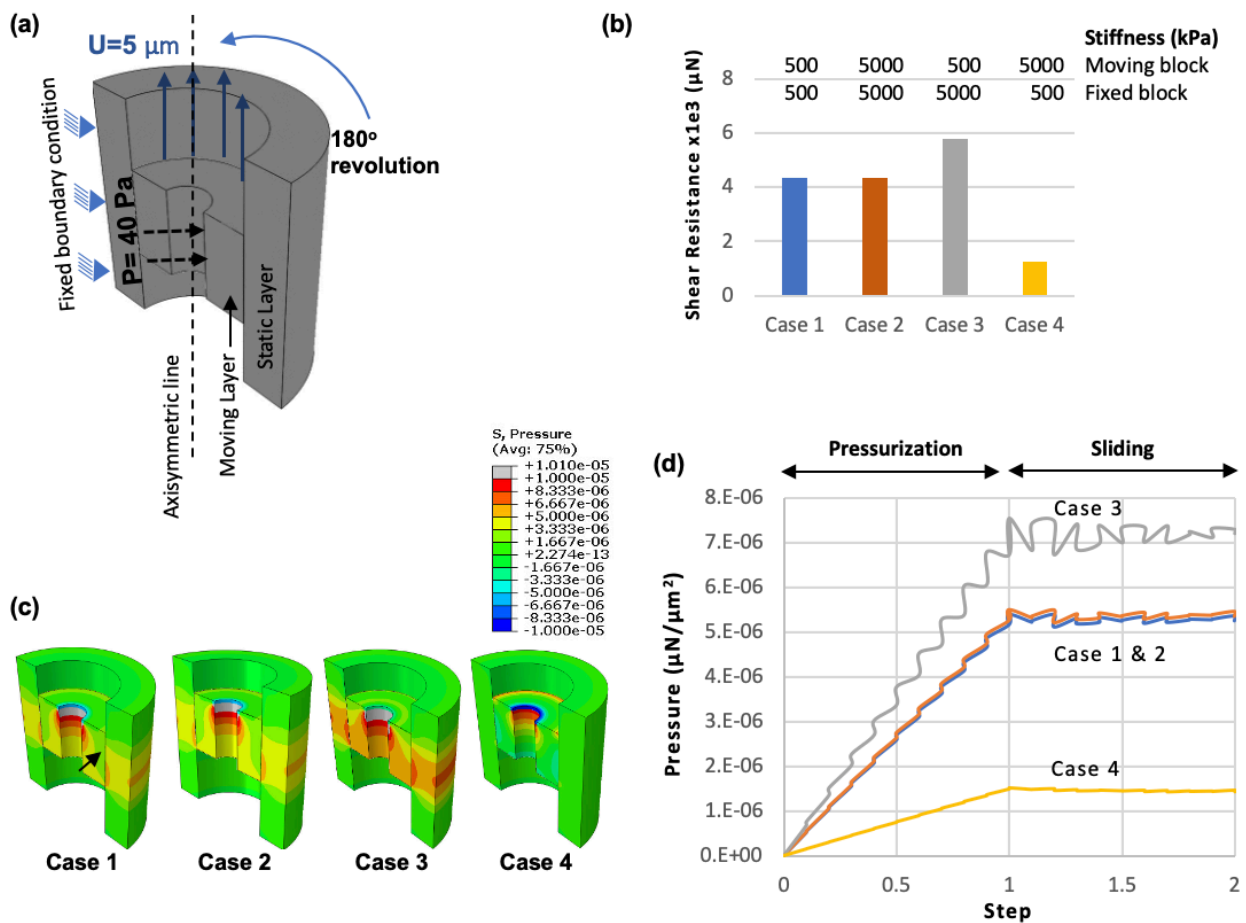
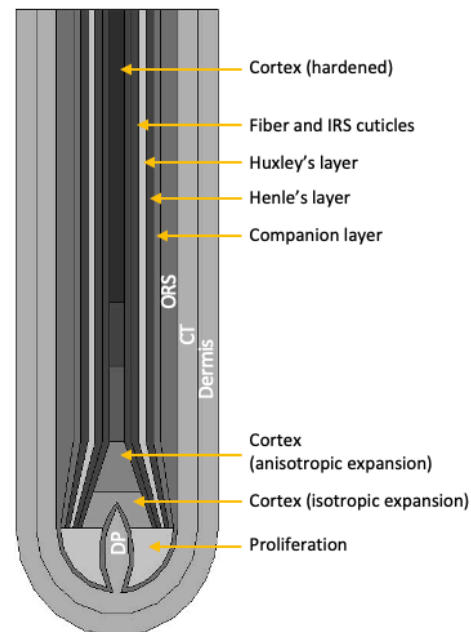


Figure 4. Two-body shear-sliding model with various combinations of material stiffness. (a) Design of the structure consisting of inner moving layer and outer static layer. The static layer is fixed at the outer surface (blue arrow heads). U (or U_2) indicates the direction of the movement of the moving layer and P indicates the pressure applied normal to the inner cylindrical wall. (b) Shear resistance generated by the moving block for four different combinations of layer stiffness identified as Cases 1-4 (c,d). Arrow in (c) indicates location at which interface pressure is monitored to produce graph shown in (d). The heat map indicates pressure values for a sliding distance of $5 \mu\text{m}$ executed by the moving layer relative to the fixed layer.

values assigned to ORS and CP (Table 1), the higher value was set to differ by one order of magnitude. The boundary conditions assigned for the simplified two-body simulations were similar to those of the hair follicle tissue model. The application of pressure and the sliding motion were executed in consecutive steps (Fig. 4a).

Table 1:
Parameters defining the mechanical properties of tissue layers

Layer	E (MPa)	Poisson's ratio
Dermis (Dr)	0.05	0.45
Connective Tissue (CT)	0.05	0.45
Outer Root Sheath (ORS)	0.5	0.45
Companion layer (CP)	0.5	0.45
Henle's layer cornified (He _c) (Z3, Z4, Zh)	1	0.45
Henle's layer bulbar (He _b) (Z1, Z2)	0.3	0.45
Huxley's layer (Hx)	0.01	0.45
Inner root sheath cuticle cornified (Ci _c)	1	0.45
Inner root sheath cuticle bulbar (Ci _b)	0.3	0.45
Fiber cuticle cornified (Cf _c)	1	0.45
Fiber cuticle bulbar (Cf _b)	0.3	0.45
Proliferation Zone (PZ)	0.01	0.45
Matrix and Pre-cortex zone (Z1)	0.1	0.45
Hair cortex elongation zone (Z2)	0.3	0.45
Hair cortex keratogenous zone lower (Z3)	0.6	0.45
Hair cortex keratogenous zone upper (Z4)	1	0.45
Hair cortex hardening zone (Zh)	10	0.38



2.2.4 Pressure to pre-stress model

To estimate the pre-defined stress generated by turgor, a cell level model was constructed, which translates cell pressure to stresses for a given domain. To this end, a cluster of 27 spherical cells with identical size, packed into a cubic lattice, surrounded by a hollow cube, was designed to represent the simplified microscale configuration of a cell cluster of living cells confined by a dermis layer (Fig. 5a). The size of the cells was derived from image analysis of cells in the hair follicle proliferation zone (PZ) (Morioka, 2005). The number 27 was chosen since it ascertains that there is at least one cell in the cluster that is surrounded entirely by other cells. With symmetric boundary conditions in all three axes, the model was solved for static analysis with application of four different pressure levels, namely: 10, 20, 30 and 40 Pa, based on the pressure levels measured in dividing HeLa cells (Fischer-Friedrich et al., 2014).

The Cauchy stress values S11, S22, S33, S12, S23, S13 were extracted at the central cell of the model (Figs. 5b,c) and these reflect the stress field of the whole domain comprised by the 27 cells. The normal stresses (S11, S22 and S33) were uniform throughout the whole domain of the cell cluster (Fig. 5b). The shear stresses (S12, S23 and S13) were extracted from the contact boundaries between two cells. The full Cauchy tensor stress was then used as input for the tissue level model as a predefined field representing the turgor induced stress for a given pressure.

2.2.5 Cellular proliferation model

The principal sources of hair fiber material and of the generation of the force pushing the protrusion of the hair shaft are the cell division occurring primarily in the basal proliferation zone (PZ), the isotropic expansion of the cells in the matrix and pre-cortex zone (Z1) and the anisotropic expansion of cells in the elongation zone (Z2) (Fig. 7a). In the tissue level model, hair follicle expansion and cellular proliferation are simulated as volume expansion characterized by the coefficient of thermal expansion (α), an intrinsic material property that relates the size change with change in temperature (T). Mathematically, the product αT measures a certain amount of volume increase representing the addition of new materials due to cellular proliferation or expansion in hair follicle. The application of temperature ($\Delta T=1^\circ$) as a boundary condition was exclusively used to simulate the change in volume in the applied domain. The material and interaction properties were decoupled from the temperature change.

In other words, the 1^o change in temperature field was solely used as a mathematical means to implement an expansion of the cellular domain. It does not affect any of the biophysical processes in the hair follicle.

After discretizing the model using CPS4R elements, static analyses were performed for different scenarios of cellular proliferation activity. The force generated due to proliferation was measured at a fixed bar restricting expansion of the proliferation zone and cell movement along the hair fiber growth direction (Fig. 6a).

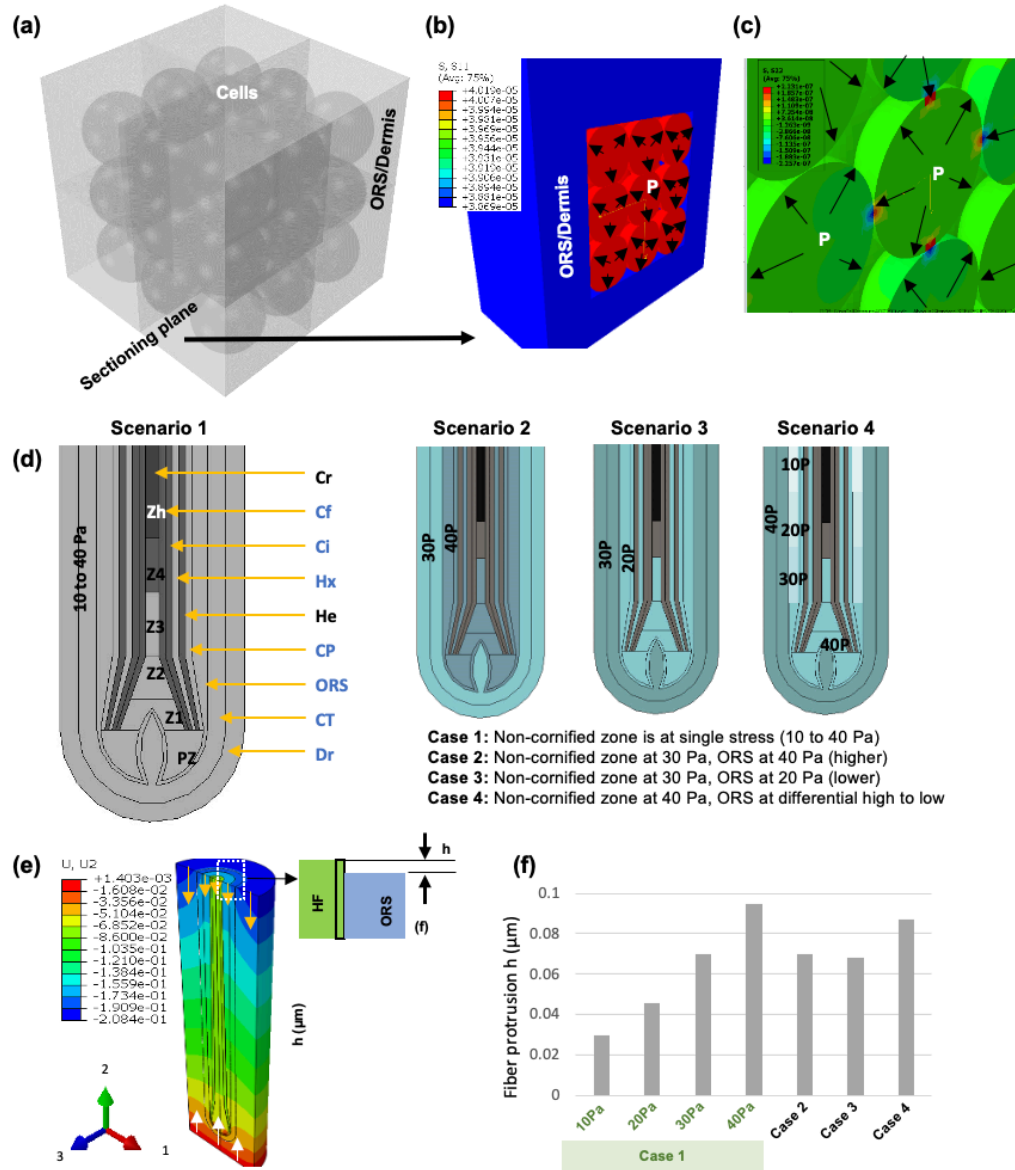


Figure 5. Pressure to pre-stress model and the contribution of zone specific differential turgor pressure to hair fiber protrusion. (a) 27-cell model used to translate turgor pressure acting on individual cell membranes into a Cauchy stress tensor in a domain constituted by these cells. (b) Sectional view of the nine-cell model showing normal stress component along direction 1 produced due to the action of 40 Pa (P). (c) Shear stress component (S12) due to 40 Pa pressure in the 27-cell model. (d) Four scenarios for pressure distribution in the non-keratogenous zones of the hair follicle. (e) Effect of pressure field on overall hair follicle shape resulting in hair fiber protrusion. White arrows show displacement of the follicle zones along the growth direction (defined as positive displacement), while orange arrows point at follicle displacement opposite to the hair growth direction (defined as negative displacement). (f) Effect of hydrostatic pressure induced pre-defined stress on hair fiber protrusion.

3 FEA model assumptions and rationale for derivation of biophysical parameters

The hair follicle consists of connective tissues, which are typically described by hyperplastic models such as Mooney-Rivlin and Neo-Hookean because their stress-strain behavior exhibits non-linearity at high deformation. However, since hair growth is very slow, it is very unlikely that any forces involved in the process result in large deformations in the follicle layers. Therefore, for the hair follicle FEA models, it was reasonable to define the constitutive laws of the discretized elements as linear elastic.

In the tissue-scale hair follicle models, connections between all tissue layers other than the CP and ORS were assumed to be tight, and relative movement at these interfaces was restricted to null. The CP-ORS boundary was defined by a specific model as detailed below (Figs. 1d,e). The effect of the transformation of the fiber cuticle from a monolayer to overlapping layers (Hashimoto, 1988) was assumed to be insignificant relative to overall hair protrusion.

The CP-ORS shear interface is known to be regulated by cadherin mediated desmosomes (Fig. 1d). During tissue morphogenesis involving cell-to-cell sliding and simultaneous maintenance of structural integrity, desmosomes play a central role (Maître and Heisenberg, 2013; Papusheva and Heisenberg, 2010). Switching between high and low affinity state signaled by protein kinase C is one of the possible mechanisms by which desmosomes regulate the dynamic adhesive attributes (Garrod and Chidgey, 2008). It is also suggested that environmental stimuli such as mechanical stress play a role in triggering signals that take part in controlling cell migration and tissue morphogenesis (Papusheva and Heisenberg, 2010).

In all FEA models, the CP-ORS interface is defined by face-to-face interaction properties, characterized by a normal and a tangential component, that reflect the biomolecular regulations of cadherin-based intercellular adhesion (Fig. 1e). The normal component of the interaction property is defined by a hard contact, which ensures that two adjacent cells do not penetrate each other. The tangential component of the interaction property is described by the coefficient of friction (COF), a dimensionless number that measures the force opposing relative movements between two adjacent layers. The value of the COF depends on the surface features (also called asperities) and the molecular adhesive behavior between two participating surfaces. Biologically, a high COF at the CP-ORS interface represents the high affinity state defined by desmosome bonding. Internal or external forces can modulate the abundance of cadherins and hence influence the COF. In addition to the COF, the shear resistance also depends on the normal force between two sliding layers (Fig. 1e). As the true mechanical nature of the CP-ORS interface is unknown, using the FEA model, we tested a wide range of COF (0-0.5) covering all reasonable scenarios associated with the regulation of intercellular adhesion.

The mathematical description of cellular proliferation or expansion in the tissue level model does not consider individual cellular boundaries or intercellular interactions, however. Between the mitotic and the elongation zones a multitude of intercellular activities takes place, including the decrease of the relative amount of intercellular space (Birbeck and Mercer, 1957), and the rotation and slippage of cells (Orwin and Woods, 1982). To assess whether simulations using a single bulk continuum/domain such as the PZ result in growth forces that are identical to those produced by a more granular approach, a cellular proliferation model was developed to simulate the lower bulb portion of the hair follicle as a cluster of individual cells. In this model, cell-to-cell interaction properties (slippage behaviour between two cells), cell size and shape, packing (the extent of the volume fraction occupied by intercellular space) and mechanical properties of cells and surrounding layers were controllable parameters (Figs. 6b-f).

In the pressure to pre-stress model, along with pressure, the average stress field induced by hydrostatic pressure in the non-cornified regions of a hair follicle depends on the material properties, size and the surroundings of a cluster of cells in each zone. These cellular and environmental parameters vary significantly across the hair follicle layers and zones. Since quantitative data are not available, wherever non-cornified cell layers or zones composed of hydrostatically active cells were located in the whole follicle model, the 27-cell cellular scale model based on the material and physical properties in the proliferation zone was used to simulate pre-defined stress.

3.1 Pre-defined stress induced by differential cellular pressures

The layers and zones in a hair follicle do not only vary in material properties and physical dimensions but also in physical and hydrostatic states of the cells (Birbeck and Mercer, 1957; Bornschlögl et al., 2016). In a hydrostatically active, living cell, the contractile forces generated by the actin-myosin network are counter balanced by the internal hydrostatic pressure (Salbreux et al., 2012). When a cell is a part of a larger domain (tissue), environmental factors such as the forces from other cells and the mechanical properties of its surroundings also become a part of the force balance (Solon et al., 2007). This tug of war at the boundary of a hydrostatically active cell creates stress which propagates from one cell to another and acts as an important signal in tissue morphogenesis (Mao and Baum, 2015). Considering that the hair follicle is composed of both non-cornified (living and pressurized) cells and cornified cells (inert cells filled with chemically crosslinked keratin and without flexible external membranes, thus lacking hydrostatic pressure (Birbeck and Mercer, 1957; Bornschlögl et al., 2016), it was critically important that the non-cornified domains of the hair follicle be assigned with stress fields generated by cellular pressure.

In the formation of the hair shaft consisting of medulla, cortex and hair fiber cuticle layers, the living isotropic cells in the bulb zone gradually transform to inert and anisotropic material while being displaced towards the distal bulb zone (Birbeck and Mercer, 1957; Bornschlöggl et al., 2016). The IRS layers cornify abruptly during maturation, but Henle's layer does so at a much earlier stage (end of elongation zone, or Orwin's threshold) compared to Huxley's layer and the IRS cuticle (Joshi, 2011). The final keratinization of the companion layer (CP) occurs at a much later stage (near the bulge zone) compared to hair shaft and other IRS layers (Ito, 1986). On the static side, the ORS stays non-keratinized over the entire lower portion of the hair follicle and merges with the skin's epidermis (distal of the bulge zone) (Wu et al., 2003). If one neglects the layers that cornify at a much later stage, the whole hair follicle can be simplified to comprise two regions with different states of pressure. The non-cornified domain consisting of active, living cells with hydrostatic pressure. This domain includes the zones of all the follicle layers proximal to the rapid cornification of Henle's layer (Orwin's threshold) as well as the entire CP, ORS, CT and dermis layers. In addition to cornified and living cells, there are cells, rapidly filling with keratin, and transforming ready for cornification. We refer to this as the keratogenous domain, and it includes all cells of the hair shaft (cortex, cuticle and medulla), IRS cuticle and Huxley's layer distal of Orwin's threshold (Z3 and Z4). These cells are trapped within a cornified tube of Henle's cells (Fig. 5d), and have lost much, but not all of their biological function (Jones et al., 2018). It remains to be clarified at what point the cells of the keratogenous domain completely lack hydrostatic pressure, or what the mechanism of hydrostatic reduction is. Here, for simplification, we included the keratogenous domain with the cornified domain because the cytoplasmic changes and significant reduction of cytoplasm in the keratogenous zones were considered to indicate lack of substantial hydrostatic pressure.

In the moving layers of the hair follicle, soft pressurized growing cells are synthesized in the bulb zone and become progressively transformed to cornified inert cells with highly organized keratin fiber (Bornschlöggl et al., 2016). This indicates the presence of a pressure gradient between the PZ, Z1 and Z2. In addition, the water that the growing layers lose during the process of cornification is likely to be channeled centrifugally towards the static or non-growing layers of the hair follicle. It is therefore quite possible that the hydrostatic fluid pressure of the cells in the ORS will be affected by the process of growing layer cornification. Similar to the putative differential pressure zone in the growing layers, the ORS is likely to have a similar pressure gradient from proximal to distal bulb zone.

Given the complex pressure differentials that are likely to exist within the follicle, we wanted to assess how sensitive hair protrusion is to variations in the spatial distribution pattern of pressure. We used the whole follicle model to simulate the following four scenarios for the generation of pre-stress through turgor application: (1) Uniform pressure in all the non-cornified zones with pressure ranging from 10 to 40 Pa (Fig. 5d), (2) ORS at higher pressure (40 Pa) than the rest of the non-cornified zones (30 Pa) (3) ORS at lower pressure (20 Pa) than the rest of the non-cornified zones (30 Pa), (4) Varying pressure within the ORS along a longitudinal gradient with a maximum at the base and minimum at the distal end. The rest of the non-cornified zones is at uniform 40 Pa pressure. Because of its elongated shape, the pressurization of the hair follicle causes swelling in radial direction and corresponding contraction in longitudinal direction (orange and white arrows in Fig. 5e). However, the degree of contraction in U2 differs between layers with the dermis contracting more than the hair shaft resulting in a protrusion of the hair shaft from the dermis. This hair protrusion generated by pressurization was measured as displacement field output along the growth direction (U2).

Higher uniform pressure values produced linearly more hair fiber protrusion compared to lower values (Fig. 5f). Importantly, despite significant differences in the spatial distribution of pressure differentials, hair protrusion in all scenarios tested fell within the range defined by the two extreme uniform pressure distributions (uniform pressure 10 Pa and 40 Pa). This means that the simulation outcomes are not very sensitive to the exact spatial distribution of pressure differentials. Interestingly, despite the average pressure being significantly lower in Scenario 4 compared to Scenario 1 (40 Pa), hair fiber protrusion is almost as high. This suggests that the drying process involved in the generation of the keratinized hair shaft might actually be a feature that is not only structurally necessary for rigidification of the hair shaft, but also physically promotes hair fiber protrusion. Given the similarity of the results obtained with Scenario 4 and 1 (40 Pa), we surmise that it is safe to use a simple pressure distribution scenario for all simulations from here on. We chose Scenario 1 with uniform pressure (40 Pa) in the non-cornified zone for all subsequent simulations.

3.2 Voids in tissue architecture and cell size

The force that ultimately causes the hair fiber to be pushed out is generated by a combination of cell proliferation and cell growth in the PZ, Z1 and Z2. The force generated by these activities acts on all tissues located distal and external to these zones. We

term this force the proliferation force. In order to assess the putative role of cellular boundaries on the generation of the overall proliferation force, the cellular proliferation model was run for the following three scenarios: (1) PZ consists of a single continuous volume without any cellular boundaries ('no cellular boundary' configuration; Fig. 6b), (2) PZ consists of multiple cells separated by a minimal amount of void space (~0.6% of the total volume; 'cellular boundary configuration'; Fig. 6c), and (3) PZ consists of multiple cells interspersed by a significant amount of void space (~9%; void space configuration; Fig. 6d). For scenarios 2 and 3, two different cell sizes, 10 and 20 μm , were implemented (Figs. 6c-f). For each scenario, an identical amount of volume was added in PZ. For scenarios 1 and 2, addition of a unit volume of material (expansion) produced almost identical force at the fixed boundary. The same was true for simulations with different degrees of intercellular slippage resistance defined by very low to very high COF (Fig. 6g). For scenario 3 (void space configuration), addition of a unit volume produced 30% and 32% less proliferation force compared to scenarios 1 (no void space configuration) for small (10 μm) and large cells (20 μm), respectively. For compact cell architecture (cellular boundary configuration with 0.6% void), the loss of proliferation force due to the presence of voids was 4.3% and 0.8% for small and large cells, respectively. For small and large cells, two different trends for the reaction force loss due to the presence of different amounts of void were observed (Fig. 6h). When PZ was comprised of smaller cells, an increase in void space had a more substantial detrimental effect on proliferation force than when the zone consisted of bigger cells. Therefore, both extent of void space and cell size in PZ affect the proliferation force. From transmission electron micrographs it has been concluded that PZ possesses a small but significant amount of intercellular space that decreases towards Z1 and Z2 (Birbeck and Mercer, 1957). In this context, it is interesting to note that cell size increases from PZ to Z1 and Z2. According to the model predictions, the reduction of void space and increase of cell size both are biomechanical mechanisms that promote the production of proliferating force. In addition, the results indicate that for a very low amount of void space and within the range tested, the presence of cellular boundaries alone is not a contributing factor to cellular proliferation force. Given that Z1 and Z2 are virtually devoid of void space and PZ harbors a very small amount of intercellular space (Morioka, 2005), the simulations suggest that in the interest of modeling simplifications, it is safe to adopt a domain expansion approach to represent proliferation or expansion of a cluster of cells in the tissue level simulations.

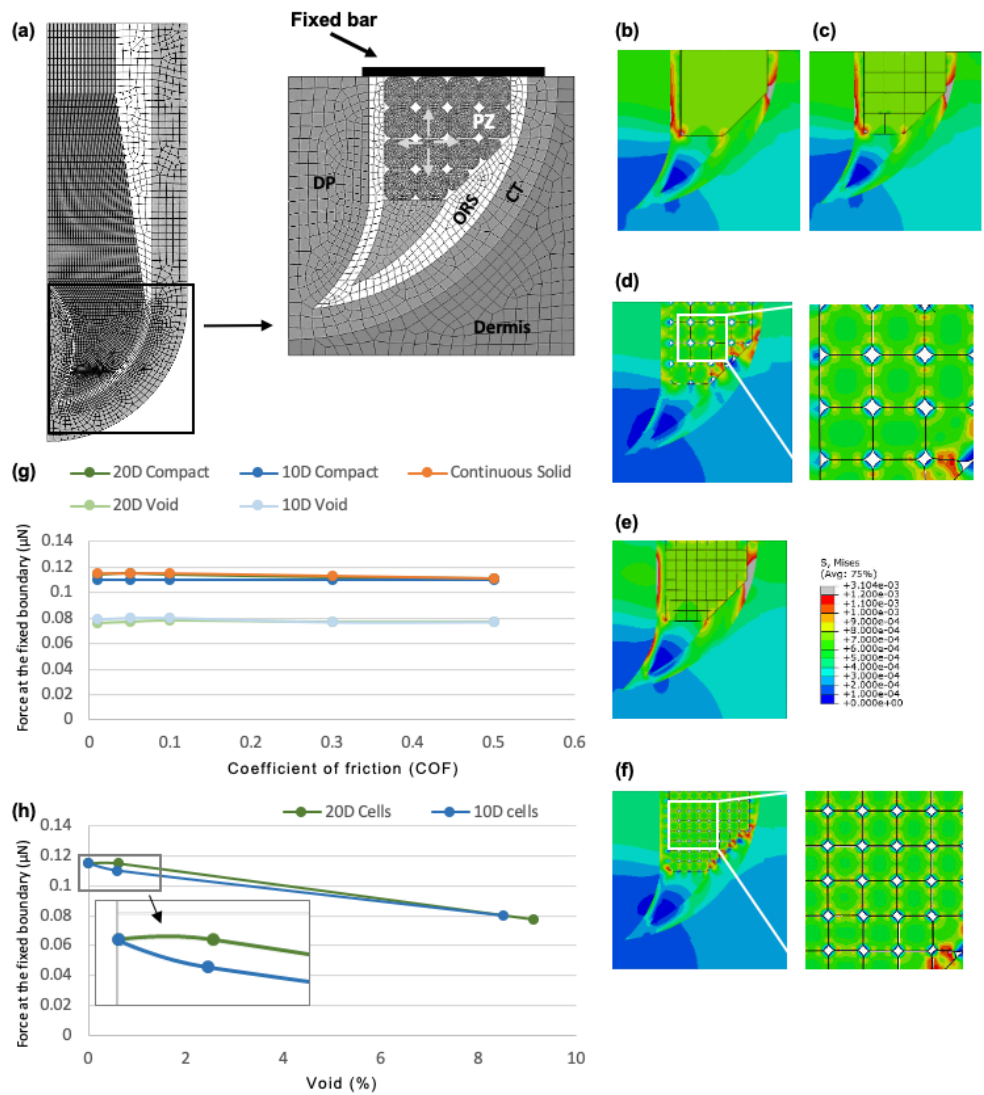


Figure 6. Proliferation and expansion at cellular scale. (a) 2D FEA model for the investigation of cellular proliferation at microscale. (b-f) von Mises stress distribution in cellular proliferation zones for the PZ as a cluster (b) without cellular boundary, (c-f) with cellular boundaries consisting of (c,d) large (20 μm) or (e,f) small (10 μm) cells with either <1% void or ~9% void. (g) Proliferation force at fixed distal boundary of PZ for different tissue architectures over a range of COF. (h) Effect of proportion of void space in PZ on proliferation force.

Interestingly, the void space configuration was found to produce bands of stress concentration zones at the intercellular junctions, which were absent in the very highly packed cellular configuration (Figs. 6d,f). The change in the amount of intercellular voids from PZ to Z1 is associated with an increasing degree of desmosome-correlated intercellular bonding (Birbeck and Mercer, 1957). Although not much is known regarding the exact regulatory mechanisms controlling the degree of desmosome activity, the generally accepted understanding is that elevated intercellular movement should correlate with the incorporation of more desmosomes. Our simulation results suggest that the presence of intercellular voids results in stress concentration zones at cell-cell interaction surfaces, which might be a triggering mechanism for the cell to initiate the deployment of new desmosomes. This inference is consistent with our understanding of cell-to-cell dynamic adhesive behavior, thought to be regulated by a local tension-induced force feedback loop (Papusheva and Heisenberg, 2010). The stress concentration-triggered force feedback loop might also be critical for regulated packaging of proliferated cells. The packaging of proliferated cells is recognized as very strictly controlled and different from passive packaging based on optimization of surface energy or space (Gibson et al., 2006).

In summary, according to our model predictions, both cell size and void spaces affect the cellular proliferation force and are likely to play an important role in regulating the mechanodynamics of cellular movements. For the same amount of cellular expansion, the larger cells produce more proliferation force compared to the smaller cells. Therefore, for the same amount of energy invested in hair fiber mass synthesis, multiplication of cells combined with subsequent increase in size is more advantageous than mere multiplication of cells and pushing them upward. As PZ is the primary cell division site, cell size is smallest here. PZ also accommodates a higher amount of intercellular void space, which according to our model prediction is likely to play a critical role for cellular organization and movement. At a given volume fraction of void space, this trait is more detrimental when cells are smaller compared to larger cells. While the small cell size seems inevitable in PZ because of the rapid cell division activity, the tendency for cells to rapidly increase size when moving towards Z1 and Z2, concomitantly to reducing the amount of void space between them, is beneficial for efficient hair protrusion.

3.3 Sensitivity of hair protrusion to bulb shape

Geometrically, hair follicles consist of a spherical-shaped bulb and a cylindrical-shaped shaft. However, depending on the source (species, location on body surface), overall hair follicle shape varies quite substantially, in particular with respect to the transition between bulb and shaft. To assess the potential effect of the shape of the transition zone, the bulb model was solved with three different transition lengths for 6% expansion of PZ (Fig. 3a). The simulation results predict that at transition lengths of twice and 1.5 times the size of the bulb radius, hair fiber protrusion is identical for the whole range of COF (Fig. 3b), whereas hair protrusion was abruptly reduced when the transition length was less than the inner radius of the ORS/bulb (Fig. 3c). We conclude that as long as the transition length is at least 1.5 times that of the radius of the bulb, the protrusion force is insensitive to the transition length. This is consistent with shape analyses done on published micrographs which indicated that the transition length is always more than twice the diameter of the bulb.

3.4 Stiffness of layers forming the sliding interface

Hair protrusion involves shear sliding of a cluster of moving layers against a cluster of static layers (Fig. 4a). To understand this shear sliding behavior, a simplified two-body FEA model was solved for 4 combinations of material stiffness (Figs. 4b-d). The two-body simulations for scenarios 1 and 2 revealed that the shear resistance at the moving-static interface remains unaffected by a change in the order of magnitude of the stiffness as long as both layers were assigned the same stiffness value (Fig. 4b). However, there was a significant change in shear resistance in case of a mismatch, when moving and static blocks were assigned different stiffness values (Fig. 4b). When the moving layer was assigned higher stiffness, resistance to sliding decreased, whereas when the moving block was assigned lower stiffness, shear resistance increased. The simulations therefore suggest that in a two-body shear sliding situation in which the sliding body is subject to a compressive force, a stiff moving layer can lead to reduction in shear resistance. This indicates that not only the material properties, but also the boundary conditions are important.

To investigate why a mismatch in stiffness with the softer body fixed leads to lower shear resistance, we monitored the pressure at the centre point of the interface between the two bodies (black arrow in Fig. 4c). The simulations showed that the pressure during both pressurization and sliding steps is affected by the combination of material stiffness values. Even with the same pressure applied to the moving layer, the interface pressure varied depending on the stiffness values. After the pressurization step, the mismatched material stiffness combination with the softer body being fixed (scenario 4) produced the lowest and the mismatched material combination with stiffer body being fixed (scenario 3) produced the highest interfacial pressure (Figs. 6c,d). When the blocks had identical stiffness, whether low (500 kPa) or high (5000 kPa), the pressurization step created identical interface pressure, the value of which was between the interfacial pressure values of scenarios 3 and 4. For all scenarios, the

interfacial pressure was found to remain constant during the sliding step. Taken together, these simulations suggest that even if the same pressure is applied on the moving block in all scenarios, the combination of material properties and their boundary conditions strongly influence the pressure generated at the interface, which in turn results in a difference in shear resistance. Except for the cortex layer, the set of material properties that were used for FEA simulations were based on educated judgement. No experimental values are available in literature. In a shear sliding pair of layers with same material stiffness, the insensitivity of the magnitude of stiffness to shear sliding behavior reduces uncertainty in the follicle scale model. As long as the material stiffness of the shear sliding pair (CP-ORS) is set to be the same for both layers, their magnitude would not affect the overall hair fiber protrusion value. From here on, this strategy was exploited unless otherwise mentioned.

4 Biomechanical factors that influence proliferation-induced hair fiber protrusion

The results of cell scale and bulb models established the framework to investigate the biomechanical factors influencing proliferation induced hair fiber protrusion. In an anagen hair follicle, the mass/volume that is synthesized/added in the proliferation and expansion zones are the primary source of hair shaft material emerging from the follicle. Any addition of mass/volume added to the proliferation and expansion zones will generate the protrusion of a certain amount of hair fiber. The extent of hair fiber protrusion is likely to vary substantially depending on the physical and mechanical properties of the follicle layers, morphogenesis mediated mechanical stiffening of different zones in a particular layer, spatiotemporal addition of new mass in the bulb zone, and the behavior of the CP-ORS shear interface.

In order to assess proliferation-mediated hair protrusion, simulations were carried out using the whole follicle model for a range of CP-ORS shear resistance mathematically described by COF 0.01 to 0.5. For a given boundary condition, the simulations included pre-stressing of the non-cornified zones of the hair follicle corresponding to 40 Pa pressure and subsequent volumetric expansion in the bulb zone, i.e., collectively in PZ, Z1 and Z2, by a set amount. The volumetric expansion has two effects – it pushes the moving layers out of the follicle in growth direction, and it expands the peripheral layers of the follicle to build up internal elastic energy. The difference in displacement of the hair fiber tip along the growth direction (direction 2) relative to the distal boundary of the static layers represents the amount of hair protrusion (Fig. 7b). The simulations showed that an increase in volumetric expansion from 5 to 7% in the bulb zone affects hair fiber protrusion in a linear manner (Fig. 7c). From here on, unless indicated differently, hair fiber protrusion simulations were carried out based on a 6% increase in volume in the bulb zone. It was also observed that for a 6% volume expansion in the bulb zone, hair fiber protrusion was significant for the full range of COF considered. For COF 0.01 to 0.5, a 6% volume expansion at the bulb zone was able to produce 0.32 (32%) to 0.06 (6%) unit fiber protrusion. This means that the remainder of the displacement occurs as elastic expansion of the bulb, primarily in direction 1.

4.1 Synthesis of material is most productive when it occurs in the proliferation zone

Fig. 7d shows the hair fiber protrusion for a range of shear interface resistance (COF 0.01 to 0.5) when PZ, Z1 and Z2 are expanded by adding a unit amount of volume equivalent to 6% of PZ. This unit amount is either added to individual zones or distributed over all three. The co-efficients of expansion of the zones were adjusted accordingly. Boundary conditions were set to ensure that PZ and Z1 expanded isotropically, whereas Z2 was set to expand anisotropically at a ratio of 10:1 (Fig. 7a). Despite the identical amount of volume added in all scenarios, hair protrusion resulting from this addition differed depending on where the material was added (Fig. 7d). Since Z2 is closer to the protrusion boundary and predominantly expands along the growth direction, we expected it to produce the highest amount of hair fiber protrusion. Instead, a unit volume increase in PZ was found to generate more hair fiber protrusion than the same volume increase in any of the other two zones. To unravel this conundrum, we closely inspected the stress distribution in radial direction (S11) in the vicinity of the CP-ORS interface (Fig. 7e). The radial stress (S11) produced due to cellular proliferation/expansion has direct impact on the CP-ORS shear interface behavior, and is thus correlated with hair fiber protrusion. It appears that because of its location just proximal to the onset of the differentiation of IRS layers, an expansion in PZ can be transferred directly to subsequent zones in vertical direction (direction 2). Expansion in PZ, therefore, produces much less radial stress at the CP-ORS interface than expansion in Z1 and Z2 (Fig. 7e). On the contrary, because of their spatial locations distal to the initiation of the IRS layers, expansion in Z1 or Z2 not only pushes the hair fiber in vertical direction, but also squeezes the IRS layers radially against the static ORS layer, which in turn increases the compressive radial stresses at the CP-ORS interface. Therefore, from a mechanical point of view, PZ seems to be the most efficient zone to add new material as it creates no counteracting effects through friction. The addition of material in Z1 and Z2 has to be optimized to ensure that the shear opposing growth is minimally affected by the expansion in radial direction.

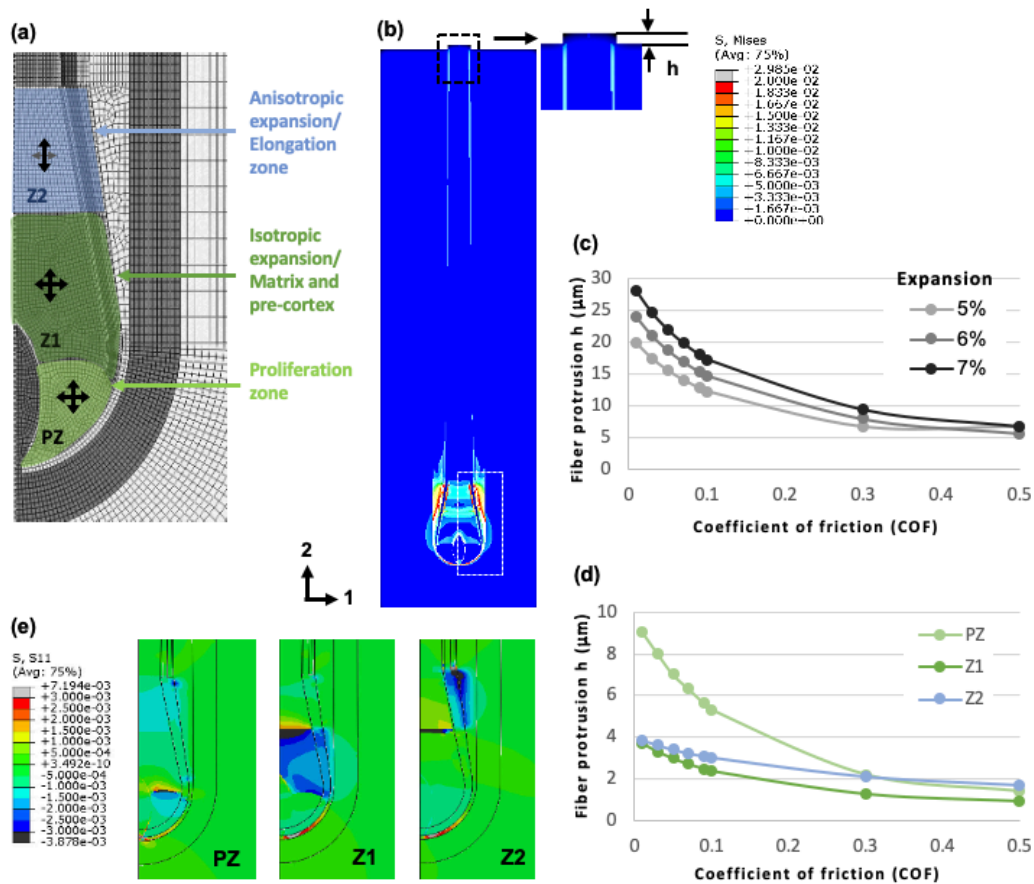


Figure 7. (a) Three hair follicle zones that are likely to contribute to the generation of hair fiber protrusion force. In the proliferation zone (PZ), the cells divide and expand isotropically; in the matrix and pre-cortex zone (Z1), the cells expand isotropically; in the elongation zone (Z2), the cells grow anisotropically. (b) Hair fiber protrusion simulation showing von Mises stress distribution in the whole follicle model for COF 0.01. Volume in PZ, Z1 and Z2 was expanded by 6% and hair fiber protrusion (h) was measured along the fiber growth direction (direction 2). (c) Hair protrusion at different volume expansion in the three follicle zones simulated with the whole follicle model. At low COF (0.01), the gradual increase in volume expansion linearly increases hair fiber protrusion. However, at a very high COF value (0.5), all three volume expansion values tested produce almost identical hair fiber protrusion. (d) Hair protrusion generated by 6% expansion applied to individual zones in the whole follicle model. (e) Stress distribution S11 in bulb zone due to proliferation and expansion in PZ, Z1 or Z2 in radial direction (direction 1). Shear resistance at CP-ORS interface is primarily influenced by S11.

4.2 Narrowing down the value for coefficient of friction

One of the most critical parameters and yet entirely unknown is the value of the COF at the CP-ORS interface. This is the reason why in all simulations done so far, we used a large sweep of that parameter space. Our abovementioned assumption for a COF in the mid-range is based on the premise that the actual value is likely to be an optimum that has to reconcile two requirements: a low COF would facilitate hair fiber protrusion, but it also minimizes the hair fiber's resistance to pulling and might therefore compromise the mechanical anchoring stability against external pulling stress. A high COF would provide maximum anchoring stability but would reduce the efficiency of hair fiber protrusion (Fig. 7).

4.3 The effect of follicle layer mechanical properties on hair fiber protrusion

The formation and progressive restructuring of keratin fiber in the hair follicle cortex layer results in a gradient of material stiffness (Baltenneck et al., 2000). The stiffness gradient in the cortex layer is particularly dramatic within the first millimeters where stiffness increases by a factor 360 (Bornschlögl et al., 2016). While the gradual stiffening of the cortex layer is fundamentally associated with hair shaft formation, it is also likely to influence hair protrusion. Like the hair shaft, the IRS layers display differential material properties along the growth direction. Consistent with their different roles in the formation of the hair shaft, Henle's layer cornifies at a very early stage whereas Huxley's layer does so at a later stage. Presumably, the IRS layers play a role in shaping, forming, and protecting the cortex layer and in facilitating hair shaft protrusion. In the whole follicle model, different arrangements of material properties were implemented to assess their respective effects on hair shaft protrusion and hair anchoring.

4.3.1 Gradual stiffening of the hair cortex layer is likely to assist hair protrusion

In the hair cortex bulb zone, cells gradually stiffen when transitioning from PZ through Z1, Z2 and Z3. To assess the effect of the gradual change in material properties in the cortex layer approaching Z3 (where Henle’s layer hardens) on hair shaft protrusion, simulations were carried out based on varying the elastic modulus of Z1: (a) same as the PZ (10 kPa); (b) higher than PZ zone (100 kPa); (c) same as Z2 (300 kPa) (Fig. 8a). Scenario b represents a two-step gradual change in material stiffness (10 to 100 to 300 kPa) during the transition from PZ to Z2, whereas scenarios a and c represent a one-step sudden change in material stiffness (10 to 300 kPa). The simulation results show that scenario b produces the highest amount of hair protrusion for the same amount of volume addition in the proliferation and expansion zones (Figs. 8a,b). This suggests that a gradual change in properties is more favorable for hair fiber protrusion compared with a sudden jump in properties.

4.3.2 Relative stiffness at the CP-ORS interface affects hair fiber protrusion

Earlier we showed that for a simplified two-body shear sliding model, material stiffness plays a critical role in regulating shear sliding behavior. Our aim was to assess if a similar relationship exists at the moving-static interface of the whole follicle model, where both moving and static sides consist of multiple layers with varying material stiffness. To this end, simulations were carried out, where the elastic moduli of CP and ORS were either kept the same while varying the value applied (50, 500 and 5000 kPa) or they were set to differ by one order of magnitude between them. When the material stiffness values of CP and ORS were kept the same, hair fiber protrusion was more pronounced at lower stiffness (Fig. 8c). With an increase of the stiffness of both layers forming the CP-ORS interface from 50 to 500 and 5000 kPa, hair fiber protrusion decreased for the whole range of

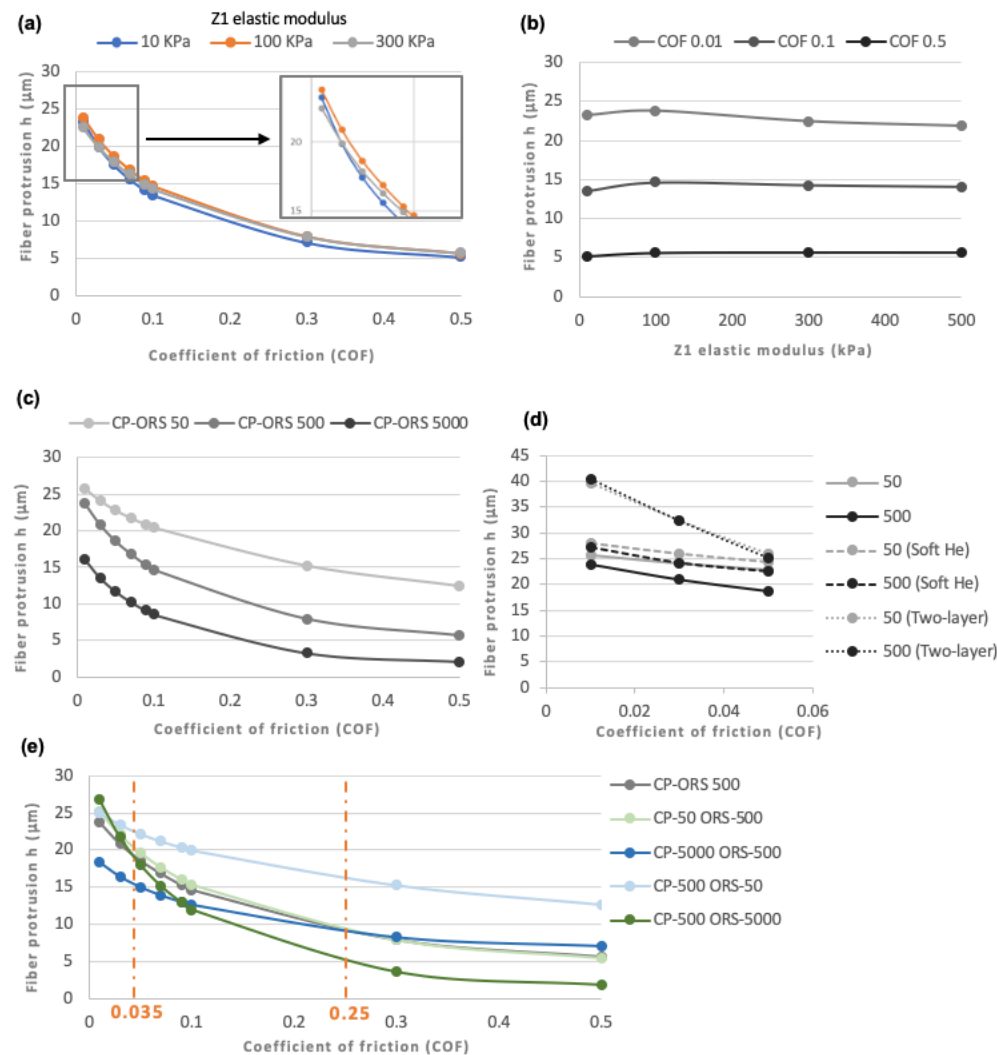


Figure 8. Effect of hair follicle layer stiffening on hair fiber protrusion predicted by the whole follicle model. (a) Effect of gradual stiffening of the hair fiber cortex on hair protrusion. Hair fiber protrusion with Z1 (cortex and pre-cortex zone) elastic modulus same as (10 kPa) or higher (100, 300 and 500 kPa) than the PZ at different CP-ORS shear resistance. (b) Hair fiber protrusion at different elastic moduli of Z1. (c) Effect of CP-ORS stiffness on hair fiber protrusion. The stiffnesses of CP and ORS were kept identical but varied between 50, 500 and 5000 kPa. (d) Effect of CP-ORS stiffness with softened He layer and homogenized properties of the moving layers and the static layers in the whole follicle model. (e) Effect of stiffness mismatch in CP-ORS interface on hair fiber protrusion simulated with the whole follicle model (stiffness values in kPa).

COF. This result appears to be inconsistent with the two-body shear sliding simulations, where it was observed that a change of one order of magnitude in stiffness values does not affect the shear sliding behavior as long as both layers are assigned the same material stiffness. The difference in model behavior is the result of the type and location of boundary conditions which play a critical role in the overall mechanical behavior of a physical system. For the two-body shear sliding model, the pressure is applied on the outer face of the moving layer while the static layer is fixed at the opposite side of the structure (Fig. 4a). For a similar shear-sliding scenario, in the whole follicle model that distinguishes the individual layers, the follicle is constrained between an axisymmetric boundary condition at the center and a fixed boundary condition at the outer surface of the dermal layer. Because of the location of these boundary conditions, the pressure induced shear

stress at the CP-ORS interface is likely to be affected by a range of material stiffnesses that are assigned for different layers and zones. Initially, we suspected that the high stiffness of Henle's layer adjacent to the CP layer might be a dominant factor causing a difference in behavior at the CP-ORS interface of the whole follicle model compared to the two-body model. To test this, we reduced the stiffness of Henle's layer in the whole follicle model to be the same as that of the neighboring Huxley's layer (10 kPa instead of 1000 kPa) and ran the simulations with matched CP-ORS stiffnesses either at 50 or 500 kPa (Fig. 8d). Given the negligible effect of COF on the trend of hair fibre production in matched CP-ORS stiffness configurations (Fig. 8c), only a partial range of COF (from 0.01 to 0.03) was explored here. Based on the predictions by the two-body model, we expected that with a softened Henle's layer, a change in stiffness at the matched CP-ORS interface would not generate a difference in hair fiber protrusion. However, while a softer Henle's layer did indeed reduce the difference in hair fiber protrusion caused by a change in CP-ORS (dashed lines compared to solid lines in Fig. 8d), it did not eliminate it. To further explore the cause of this difference in model behavior, we eliminated all material inhomogeneity in the whole follicle model by clustering the moving layers assigning them identical material properties and assigned a second set of properties to all layers on the static side. This homogenization produced a good match between the simulations of the two-body shear sliding model and the whole follicle model since a one order of magnitude change in stiffness at the matched CP-ORS interface did not affect hair fiber protrusion anymore (dotted lines in Fig. 8d). Based on the simulation results of the aforementioned two studies, the CP-ORS interface of the whole follicle model appeared to be convoluted by the complex distribution of stiffness values in different layers and zones of the follicle. While in both two-body model and whole follicle model the behavior of the sliding interface is largely dependent upon the material properties, the configuration of material properties that leads to lesser shear resistance is likely to be different. For the whole follicle model, a softer CP-ORS pair appeared to be most favorable for hair fiber protrusion. In addition, it was also observed that the hardening of the moving layers inward from the CP, such as Henle's layer, does not affect the CP-ORS interface to a large extent.

When the stiffnesses of the two sliding layers differed, some conditions were found more favorable and others less favorable than those of the matching stiffness pair (both CP and ORS 500 kPa). The trend varied depending on the COF (Fig. 8e). Below COF 0.035, three of the simulated mismatched configurations were found to produce more hair protrusion than the matched CP-ORS configuration. Only when the stiffness of the moving layer (CP) was one order of magnitude higher than that of the static layer (ORS) was hair protrusion lower compared with the matching stiffness pair. In other words, within this low COF range, a soft moving layer (CP) was a dominant factor.

At an intermediate range of COF (0.035 to 0.25), a softened CP lost its beneficial effect for hair protrusion. Two mismatched configurations simulated here produced more and two produced less hair fiber protrusion compared to matched CP-ORS. At COF values exceeding 0.25, two mismatched conditions produced more, one approximately the same and one less hair fiber protrusion compared to matched CP-ORS. In this range (above 0.25), the stiffer moving layer (CP), was a dominant factor regulating hair fiber protrusion.

Overall, for the full range of COF, the mismatched CP-ORS configuration was found to have a higher potential to produce more hair fiber. In the two-body model, the solution for the least shear resistance at the moving-sliding interface is a unique configuration. In the whole follicle model, on the other hand, the lowest degree of shear resistance translating into maximum hair fiber protrusion could be attained by a variety of configurations. The differential distribution of material stiffness at different layers and zones is likely to be the cause of the variety of optimal solutions.

Together, the results suggest that in the CP-ORS shear sliding behavior, the stiffness of both CP and ORS play a pivotal role in mediating shear resistance. For a matched CP-ORS configuration, a softer interface was found to produce more hair fiber than a stiffer interface. However, overall, a mismatched CP-ORS pair has the potential to produce more hair fiber than a matched pair. Interestingly, for mismatched CP-ORS configurations, the effect varied significantly across the range of COF.

Because of lack of experimental data, in the follicle model, the material properties of CP and ORS layers were kept identical along the whole length of the follicle (direction 2). However, it is likely that the CP layer is subject to gradual stiffening like the rest of the growing hair fiber layers. This opens interesting conceptual avenues. Given the variability of mismatched CP-ORS pairs depending on COF, there is the potential that hair fiber protrusion could be optimized by having a changing CP stiffness accompanied by a change in COF value along the growth direction. In other words, it is possible that the shear resistance at the sliding interface gradually changes in growth direction, in concert with gradual stiffness changes in the growing layers of the hair follicle. A stiffened Henley's layer, despite its role as a protecting shell against mechanical disturbance and its ability to impart anchoring strength, was not found to interfere with hair fiber protrusion to any significant extent.

5 Conclusion

A multi-scale FEA modeling framework for hair follicles was developed in an attempt to understand the putative contributions of biomechanical forces and impedances associated with the growth of mammalian hair fiber. An overall follicle model was supported and informed by two additional tissue-scale and two cell-scale models. The supporting models served to provide inputs, justification for adopted mathematical approaches and deconvoluted the specifics of biomechanical phenomena at different length scales in the following ways: (1) the pressure to pre-stress model provided initial condition feeds; (2) the proliferation model justified the exploitation of the volumetric expansion approach as a means to represent cellular proliferation and explored the effect of tissue architecture in generating proliferation force; (3) the bulb model investigated the geometric

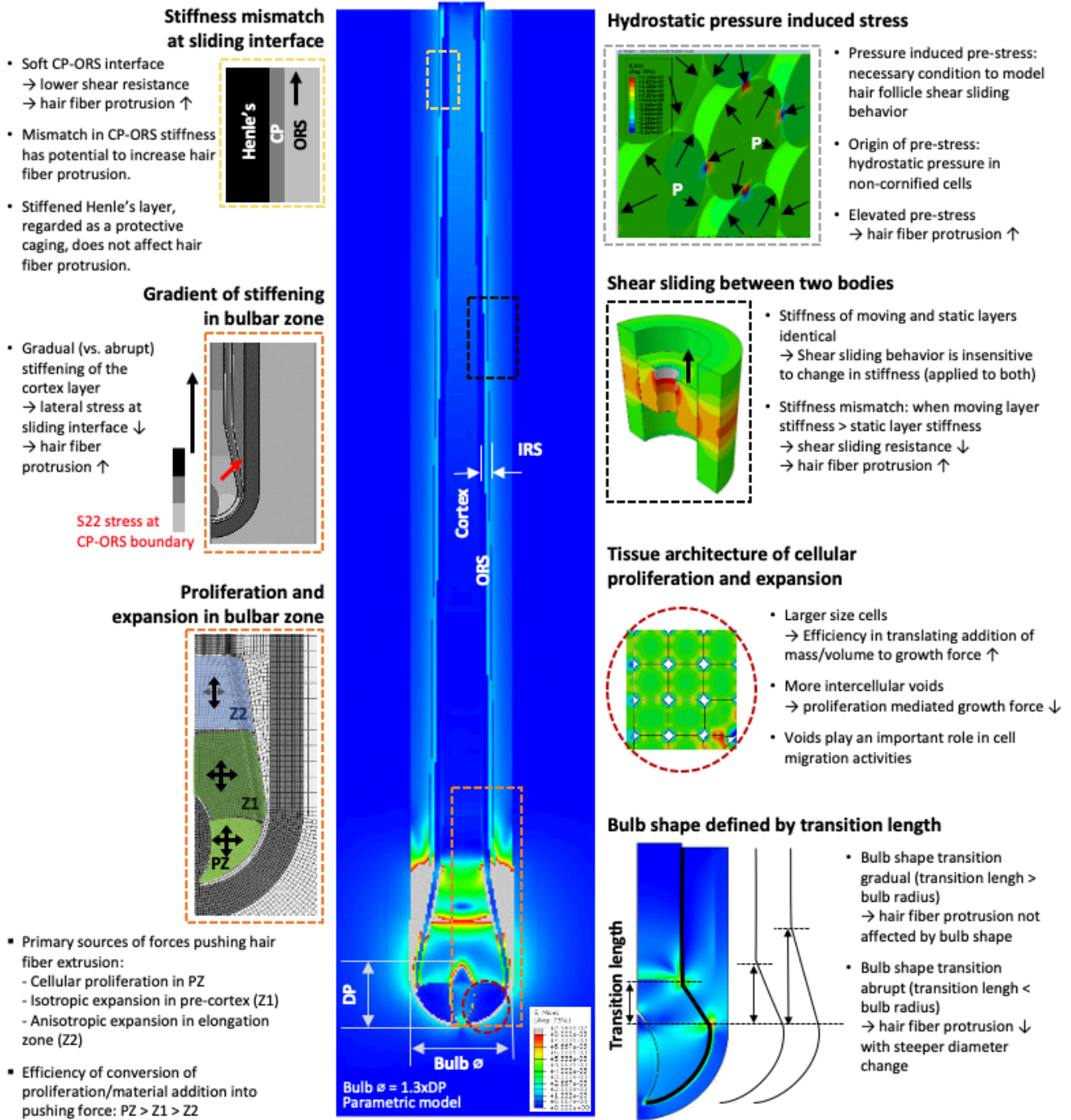


Figure 9: Summary of the predictions generated by the FEA simulations at different length scales. The models simulating cellular and subcellular events provided both input parameters for the tissue scale models and they allowed making a number of verifiable predictions relating to the relevant length scale. All predictions by the individual models are listed in bullet point format on the figure.

feature critical for channeling growth force from bulb towards the fiber protrusion direction; (4) the two-body shear sliding model explored the biomechanical underpinnings in shear sliding pairs composed of similar or different stiffness layers. The integration and relation between these models are depicted in Fig. 9.

The application of hydrostatic pressure induced pre-stress resulting from keratinization and hardening in the hair follicle model indicated that the differential pressure alone is not sufficient to generate fiber protrusion, but it provides a “down-hill slope” for other processes to push. The synthesis of material by proliferation and expansion at the bulb zone was found to produce a significant amount of protrusion of hair fiber for a wide range of COF at the CP-ORS shear interface. Even at a very high shear resistance at CP-ORS interface, the 6% volume addition at the bulb zone was able to produce 5.6 μm of fiber protrusion, which is equivalent to 6.7% of the total volume added. However, the simulation results also suggest that addition of materials in PZ, Z1 and Z2 is not equally productive in generating fiber protrusion. PZ was found most and Z2 least productive. Further investigation of proliferation in PZ indicated that the architecture of cellular arrangements (abundance of voids and cell size) affects fiber protrusion. The presence of intercellular spaces (voids), a feature that is more pronounced in PZ and gradually decreases towards Z1 and Z2, affects hair fiber protrusion negatively. Cell size, a trait that gradually increases from PZ to Z2, positively affects hair fiber protrusion. Therefore, in terms of spatial localization, PZ is the most productive whereas architecturally, Z1 and Z2 have the more favorable structural traits. Locating proliferation/cell division in PZ and confining cell expansion and compaction to Z1 and Z2, seem to combine to an ingenious strategy that optimizes the productivity of hair fiber protrusion. The intercellular voids and shapes of the cells in the bulb zone were also identified as important factors in generating stress concentration zones, a feature that is likely to regulate desmosome-correlated cellular movement. Bulb shape did not appear to have any effect on hair fiber protrusion as long as the size ratio between spherical bulb radius to cylindrical shaft transition zone length is 1.5 times or more. This seems to be the case according to all the images we analyzed for this study.

The controlled and selective hardening of the follicle layers/zones was also predicted to play an important role in hair fiber protrusion. It was observed that a gradual stiffening of the cortex layer at the proximal bulb zone assists hair fiber protrusion, suggesting that hair fiber cornification is likely to be a precisely controlled gradual process to avoid an abrupt transition. The keratinization/hardening of Henle’s layer at an early stage and different configurations of CP-ORS material stiffness were found to play an important role in balancing the requirement for lower shear resistance at the CP-ORS interface for hair protrusion with that for sufficient anchoring strength. With the assistance of a simplified two-body shear sliding model it was explored that a mismatch in stiffness with stiffer layer on the moving side significantly reduces the shear sliding resistance. Simulations performed with the whole hair follicle model confirmed that a mismatched CP-ORS configuration has the potential to produce more hair fiber protrusion. However, the trends differed depending on the COF. Based on our simulation results, we predict that the COF, a mathematical analogue of the CP-ORS shear sliding behavior, is likely subject to gradual changes during maturation (and hence along the longitudinal axis), consistent with the processes in the rest of the hair follicle moving layers, and thus ensure that hair fiber protrusion is optimized. In summary, we conclude that biomechanical factors associated with hair fiber growth are likely to play important roles in governing hair fiber protrusion in an anagen hair follicle. According to all the simulation results at different length scales, fine tuning of the biophysical parameters is critical for efficient hair fiber protrusion and the survival of hair follicle against external shocks. Combined, the predictions made by our model provide an important set of concepts with the potential to guide experiment design as well as interpretation of mutant phenotypes and pathologies in future experimental work.

6 Limitations of the model

Mathematical and computational models of biological systems can guide our understanding of the relative importance of individual parameters in a complex system. Furthermore, building a model tests our understanding of a whole system or process because sufficient detail of all sub-processes and variations within these must be included and accounted for. Generating sensible system-level results often requires having to make assumptions and generalizations which allows the identification of knowledge gaps.

Many of the data informing the follicle model came from a range of disparate studies on follicle biology, chemistry and physics. Data on mechanical stiffness were adopted from different studies than those providing information on geometric dimensions. These studies used different follicles and different preparation methods and the resulting model thus presents a “generic” human scalp hair follicle. Many of the data used for key morphological measurements (e.g., cell size, intracellular space) are from microscopy studies in which shrinkage and distortion artifacts are routine (e.g., caused by chemical fixatives and dehydration)

and three-dimensional morphology is inferred from two-dimensional slices. Our results suggest that improved precision from anatomical measurements, and also 3D volume imaging will be important for future modelling. This may require the use of sample preparation protocols with enhanced preservation of geometry such as those based on cryofixation and advanced imaging methods such as ultrastructure volume imaging. For the present generic modeling platform, it was considered that the hair follicle satisfies rotational axisymmetry. This limits the relevance of the predictions to hair follicles growing straight hair. Follicles generating wavy and curly hair have more complex geometry and the validity of the predictions made in the current study remains to be tested for these more complex follicle shapes.

Some data were not available (e.g., direct elasticity data for IRS) and educated guesses and optimization of parameters were required. The fact that the multi-scale model provides useful predictions at a scale that is realistic, suggests that the approach is useful for elucidating the role of the biomechanical phenotype for hair growth. Additional data will be needed to reliably fill knowledge gaps and to test our assumptions. They will enable future studies to assess the effect of natural variations in the microscopic and macroscopic phenotype of follicle and hair. Among the processes that warrant closer experimental analysis are cell movement and reshaping occurring within the proliferation zone (especially the IRS and CP) and during cell passage through the elongation zone, the quantitative measurement of slippage between all layers to establish whether CP-ORS is the sole interface at which slippage occurs, routes of fluid movement during the process and the quantification of the elasticity and hydrostatic pressure of the IRS, CP and ORS layers. Any active biological mechanism within the CP that affects the COF (e.g., hypothesized in (Lemasters et al., 2017) may have a particularly marked effect on the system. Understanding these fundamentals will underpin work connecting biomechanics to biological variation in fibre function (e.g., hair curvature).

Acknowledgments

This project was funded in part by Procter & Gamble. DH's contribution was also supported by AgResearch through its Smart and Sustainable Biomaterials Programme (New Zealand Government Ministry of Business Innovation & Employment, Science strategic investment fund). Research in the Geitmann lab is also supported by a Discovery Grant from the Natural Sciences and Engineering Research Council of Canada and the Canada Research Chairs Program.

References

- Baltenneck, F., Bernard, Garson, J.C., Engstrom, P., Riekel, C., Leroy, F., Franbourg, A., Doucet, J., 2000. Study of the keratinization process in human hair follicle by X-ray microdiffraction. *Cell. Mol. Biol. (Noisy-le-grand)*. 46, 1017–1024.
- Birbeck, M., Mercer, E., 1957. The electron microscopy of the human hair follicle: part 1. introduction and the hair cortex. *J. Cell Biol.* 3, 203–214. <https://doi.org/10.1083/jcb.3.2.203>
- Bornschlögl, T., Bildstein, L., Thibaut, S., Santoprete, R., Fiat, F., Luengo, G.S., Doucet, J., Bernard, B.A., Baghdadli, N., 2016. Keratin network modifications lead to the mechanical stiffening of the hair follicle fiber. *Proc. Natl. Acad. Sci.* 113, 5940–5945. <https://doi.org/10.1073/PNAS.1520302113>
- Brodland, G.W., 2015. How computational models can help unlock biological systems. *Semin. Cell Dev. Biol.* 47–48, 62–73. <https://doi.org/10.1016/j.semcdb.2015.07.001>
- Brodland, G.W., 2004. Computational modeling of cell sorting, tissue engulfment, and related phenomena: A review. *Appl. Mech. Rev.* 57, 47–76.
- Dintwa, E., Jancsó, P., Mebatsion, H.K., Verlinden, B., Verboven, P., Wang, C.X., Thomas, C.R., Tijskens, E., Ramon, H., Nicolaï, B., 2011. A finite element model for mechanical deformation of single tomato suspension cells. *J. Food Eng.* 103, 265–272. <https://doi.org/10.1016/j.jfoodeng.2010.10.023>
- Ebling, F.J.G., 1991. Hormones and hair growth, in: *Physiology, Biochemistry, and Molecular Biology of the Skin*. Oxford university press, Ney York, pp. 660–696.
- Fayant, P., Girlanda, O., Chebli, Y., Aubin, C.-É., Villemure, I., Geitmann, A., 2010. Finite element model of polar growth in pollen tubes. *Plant Cell Online* 22, 2579–2593. <https://doi.org/10.1105/tpc.110.075754>
- Fischer-Friedrich, E., Hyman, A.A., Jülicher, F., Müller, D.J., Helenius, J., 2014. Quantification of surface tension and internal pressure generated by single mitotic cells. *Sci. Rep.* 4, 6213.
- Garrod, D., Chidgey, M., 2008. Desmosome structure, composition and function. *Biochim. Biophys. Acta - Biomembr.* 1778, 572–587. <https://doi.org/10.1016/J.BBAMEM.2007.07.014>
- Gibson, M.C., Patel, A.B., Nagpal, R., Perrimon, N., 2006. The emergence of geometric order in proliferating metazoan epithelia. *Nature* 442, 1038.
- Greenberg, D.A., Fudge, D.S., 2013. Regulation of hard α -keratin mechanics via control of intermediate filament hydration: matrix squeeze revisited. *Proc. R. Soc. B Biol. Sci.* 280, 20122158. <https://doi.org/10.1098/rspb.2012.2158>
- Hanakawa, Y., Li, H., Lin, C., Stanley, J.R., Cotsarelis, G., 2004. Desmogleins 1 and 3 in the companion layer anchor mouse anagen hair to the follicle. *J. Invest. Dermatol.* 123, 817–822. <https://doi.org/10.1111/J.0022-202X.2004.23479.X>
- Harland, D.P., 2018. Introduction to hair development. *Adv. Exp. Med. Biol.* 1054, 89–96. https://doi.org/10.1007/978-981-10-8195-8_8
- Harland, D.P., Plowman, J.E., 2018. Development of Hair Fibres. *Adv. Exp. Med. Biol.* 1054, 109–154. https://doi.org/10.1007/978-981-10-8195-8_10
- Hashimoto, K., 1988. The structure of human hair. *Clin. Dermatol.* 6, 7–21. [https://doi.org/10.1016/0738-081X\(88\)90060-0](https://doi.org/10.1016/0738-081X(88)90060-0)
- Ito, M., 1986. The innermost cell layer of the outer root sheath in anagen hair follicle: light and electron microscopic study. *Arch. Dermatol. Res.* 279, 112–119.

- Jimenez, F., Izeta, A., Poblet, E., 2011. Morphometric analysis of the human scalp hair follicle: practical implications for the hair transplant surgeon and hair regeneration studies. *Dermatologic Surg. Off. Publ. Am. Soc. Dermatologic Surg.* [et al.] 37, 58–64. <https://doi.org/10.1111/j.1524-4725.2010.01809.x>
- Jones, L.A., Harland, D.P., Jarrold, B.B., Connolly, J.E., Davis, M.G., 2018. The walking dead: sequential nuclear and organelle destruction during hair development. *Br. J. Dermatol.* 178, 1341–1352. <https://doi.org/10.1111/bjd.16148>
- Joshi, R.S., 2011. The inner root sheath and the men associated with it eponymically. *Int. J. Trichology* 3, 57–62. <https://doi.org/10.4103/0974-7753.82119>
- Kam, Y., Rejniak, K.A., Anderson, A.R.A., 2012. Cellular modeling of cancer invasion: integration of in silico and in vitro approaches. *J. Cell. Physiol.* 227, 431–438. <https://doi.org/10.1002/jcp.22766>
- Langbein, L., Rogers, M.A., Praetzel, S., Aoki, N., Winter, H., Schweizer, J., 2002. A novel epithelial keratin, hK6irs1, is expressed differentially in all layers of the inner root sheath, including specialized huxley cells (Flugelzellen) of the human hair follicle. *J. Invest. Dermatol.* 118, 789–799. <https://doi.org/10.1046/j.1523-1747.2002.01711.x>
- Langbein, L., Rogers, M.A., Winter, H., Praetzel, S., Schweizer, J., 2001. The catalog of human hair keratins: II. expression of the six type ii members in the hair follicle and the combined catalog of human type I and II keratins. *J. Biol. Chem.* 276, 35123–35132. <https://doi.org/10.1074/jbc.M103305200>
- Lemasters, J.J., Ramshesh, V.K., Lovelace, G.L., Lim, J., Wright, G.D., Harland, D., Dawson, T.L.J., 2017. Compartmentation of mitochondrial and oxidative metabolism in growing hair follicles: A ring of fire. *J. Invest. Dermatol.* 137, 1434–1444. <https://doi.org/10.1016/j.jid.2017.02.983>
- Lim, Y.S., Harland, D.P., Dawson Jr, T.L., 2019. Wanted, dead and alive: Why a multidisciplinary approach is needed to unlock hair treatment potential. *Exp. Dermatol.* 28, 517–527. <https://doi.org/10.1111/exd.13898>
- Maître, J.-L., Heisenberg, C.-P., 2013. Three functions of cadherins in cell adhesion. *Curr. Biol.* 23, R626–R633. <https://doi.org/10.1016/j.cub.2013.06.019>
- Mao, Y., Baum, B., 2015. Tug of war—The influence of opposing physical forces on epithelial cell morphology. *Dev. Biol.* 401, 92–102. <https://doi.org/10.1016/j.ydbio.2014.12.030>
- Morioka, K., 2005. Hair follicle: differentiation under electron microscope: an atlas. Springer, Tokyo.
- Oh, J.W., Klopper, J., Langan, E.A., Kim, Y., Yeo, J., Kim, M.J., Hsi, T.-C., Rose, C., Yoon, G.S., Lee, S.-J., Seykora, J., Kim, J.C., Sung, Y.K., Kim, M., Paus, R., Plikus, M. V., 2016. A Guide to Studying Human Hair Follicle Cycling In Vivo. *J. Invest. Dermatol.* 136, 34–44. <https://doi.org/https://doi.org/10.1038/JID.2015.354>
- Orwin, D.F., 1971. Cell differentiation in the lower outer sheath of the Romney wool follicle: a companion cell layer. *Aust. J. Biol. Sci.* 24, 989–999.
- Orwin, D.F., Woods, J.L., 1982. Number changes and development potential of wool follicle cells in the early stages of fiber differentiation. *J. Ultrastruct. Res.* 80, 312–322.
- Papusheva, E., Heisenberg, C.-P., 2010. Spatial organization of adhesion: force-dependent regulation and function in tissue morphogenesis. *EMBO J.* 29, 2753–2768. <https://doi.org/10.1038/emboj.2010.182>
- Piecznyek, P.M., Zdunek, A., 2014. Finite element modelling of the mechanical behaviour of onion epidermis with incorporation of nonlinear properties of cell walls and real tissue geometry. *J. Food Eng.* 123, 50–59. <https://doi.org/10.1016/j.jfoodeng.2013.09.012>
- Plowman, J.E., Harland, D.P., Ganeshan, S., Woods, J.L., van Shaijik, B., Deb-Choudhury, S., Thomas, A., Clerens, S., Scobie, D.R., 2015. The proteomics of wool fibre morphogenesis. *J. Struct. Biol.* 191, 341–351. <https://doi.org/10.1016/j.jsb.2015.07.005>
- Rayfield, E.J., 2007. Finite element analysis and understanding the biomechanics and evolution of living and fossil organisms. *Annu. Rev. Earth Planet. Sci.* 35, 541–576. <https://doi.org/10.1146/annurev.earth.35.031306.140104>
- Reddy, J.N., 1993. An introduction to the finite element method. McGraw-Hill New York.
- Richmond, B.G., Wright, B.W., Grosse, I., Dechow, P.C., Ross, C.F., Spencer, M.A., Strait, D.S., 2005. Finite element analysis in functional morphology. *Anat. Rec. Part A Discov. Mol. Cell. Evol. Biol.* 283, 259–274.
- Saitoh, M.M., 1969. Rate of hair growth, in: *Advances in Biology of Skin*. Pergamon Press, Ney York, pp. 183–202.
- Salbreux, G., Charras, G., Paluch, E., 2012. Actin cortex mechanics and cellular morphogenesis. *Trends Cell Biol.* 22, 536–545. <https://doi.org/10.1016/j.tcb.2012.07.001>
- Sanati Nezhad, A., Geitmann, A., 2013. The cellular mechanics of an invasive lifestyle. *J. Exp. Bot.* <https://doi.org/10.1093/jxb/ert254>
- Sanati Nezhad, A., Naghavi, M., Packirisamy, M., Bhat, R., Geitmann, A., 2013. Quantification of cellular penetrative forces using lab-on-a-chip technology and finite element modeling. *Proc. Natl. Acad. Sci. U. S. A.* 110, 8093–8098. <https://doi.org/10.1073/pnas.1221677110>
- Schneider, M.R., Schmidt-Ullrich, R., Paus, R., 2009. The Hair Follicle as a Dynamic Miniorgan. *Curr. Biol.* 19, R132–R142. <https://doi.org/10.1016/j.cub.2008.12.005>
- Shimomura, Y., 2013. Current genetics in hair diseases, in: *Current Genetics in Dermatology*. IntechOpen. <https://doi.org/10.5772/54004>
- Solon, J., Levental, I., Sengupta, K., Georges, P.C., Janmey, P.A., 2007. Fibroblast adaptation and stiffness matching to soft elastic substrates. *Biophys. J.* 93, 4453–4461. <https://doi.org/10.1529/biophysj.106.101386>
- Stadtländer, C.T.K.-H., 2014. Cell mechanics: from single scale-based models to multiscale modelling. *J. Biol. Dyn.* 8, 74–78. <https://doi.org/10.1080/17513758.2014.901429>
- Stenn, K., Paus, R., 2001. Controls of hair follicle cycling. *Physiol. Rev.* 81, 449–494. <https://doi.org/10.1152/physrev.2001.81.1.449>
- Wang, Y., Badea, T., Nathans, J., 2006. Order from disorder: Self-organization in mammalian hair patterning. *Proc. Natl. Acad. Sci.* 103, 19800 LP – 19805. <https://doi.org/10.1073/pnas.0609712104>
- Wu, H., Stanley, J.R., Cotsarelis, G., 2003. Desmoglein isotype expression in the hair follicle and its cysts correlates with type of keratinization and degree of differentiation. *J. Invest. Dermatol.* 120, 1052–1057. <https://doi.org/10.1046/J.1523-1747.2003.12234.X>
- Yang, H., Adam, R.C., Ge, Y., Hua, Z.L., Fuchs, E., 2017. Epithelial-Mesenchymal Micro-niches Govern Stem Cell Lineage Choices. *Cell* 169, 483–496.e13. <https://doi.org/https://doi.org/10.1016/j.cell.2017.03.038>
- Yi, H., Puri, V.M., 2012. Architecture-based multiscale computational modeling of plant cell wall mechanics to examine the hydrogen-bonding hypothesis of cell wall network structure model. *Plant Physiol.* 160, 1281–92. <https://doi.org/10.1104/pp.112.201228>

Supplemental Material

Biomechanics of hair fibre growth: a multi-scale modeling approach

M. Shafayet Zamil, Duane P. Harland, Brian K. Fisher, Michael G. Davis, James R. Schwartz, Anja Geitmann

Supplemental Table S1: Sources for quantitative parameter values

Parameter	Source of quantitative values	References
Whole follicle FEA geometry	Measured from published images using parametric study approach	Langbein et al., 2001 Oh et al., 2016 Shimomura, 2013 Stenn and Paus, 2001 Wu et al., 2003
Cortex elasticity	Published data based on atomic force microscopy study	Bornschlöggl et al., 2016
Mechanical properties (elastic modulus and hydrostatic pressure) of growing cells in bulb zone	Estimated from atomic force microscopy studies on a variety of mammalian cell types	Fischer-Friedrich et al., 2014 Kuznetsova et al., 2007
Mechanical properties of IRS and ORS at different zones	No published data available. Estimations made based on educated judgement	
Mechanical properties of dermis and connective tissue	Adopted from published data on dermis tissue and/or fibroblasts. Connective tissue (dermal sheath) is composed of fibroblasts similar to the rest of the dermis	Carlsen, 1974 Liang and Boppart, 2010

References cited in Table S1

- Bornschlöggl, T., Bildstein, L., Thibaut, S., Santoprete, R., Fiat, F., Luengo, G.S., Doucet, J., Bernard, B.A., Baghdadli, N., 2016. Keratin network modifications lead to the mechanical stiffening of the hair follicle fiber. *Proc. Natl. Acad. Sci.* 113, 5940–5945.
- Carlsen, R.A., 1974. Human fetal hair follicles: The mesenchymal component. *J. Invest. Dermatol.* 63, 206–211.
- Fischer-Friedrich, E., Hyman, A.A., Jülicher, F., Müller, D.J., Helenius, J., 2014. Quantification of surface tension and internal pressure generated by single mitotic cells. *Sci. Rep.* 4, 6213.
- Kuznetsova, T.G., Starodubtseva, M.N., Yegorenkov, N.I., Chizhik, S.A., Zhdanov, R.I., 2007. Atomic force microscopy probing of cell elasticity. *Micron* 38, 824–833.
- Langbein, L., Rogers, M.A., Winter, H., Praetzel, S., Schweizer, J., 2001. The catalog of human hair keratins: II. expression of the six type ii members in the hair follicle and the combined catalog of human type I and II keratins. *J. Biol. Chem.* 276, 35123–35132
- Liang, X., Boppart, S.A., 2010. Biomechanical properties of in vivo human skin from dynamic optical coherence elastography. *IEEE Trans. Biomed. Eng.* 57, 953–959.
- Oh, J.W., Klopper, J., Langan, E.A., Kim, Y., Yeo, J., Kim, M.J., Hsi, T.-C., Rose, C., Yoon, G.S., Lee, S.-J., Seykora, J., Kim, J.C., Sung, Y.K., Kim, M., Paus, R., Plikus, M. V., 2016. A guide to studying human hair follicle cycling in vivo. *J. Invest. Dermatol.* 136, 34–44.
- Shimomura, Y., 2013. Current genetics in hair diseases, in: *Current Genetics in Dermatology*. IntechOpen. <https://doi.org/10.5772/54004>
- Stenn, K., Paus, R., 2001. Controls of hair follicle cycling. *Physiol. Rev.* 81, 449–494.
- Wu, H., Stanley, J.R., Cotsarelis, G., 2003. Desmoglein isotype expression in the hair follicle and its cysts correlates with type of keratinization and degree of differentiation. *J. Invest. Dermatol.* 120, 1052–1057.

Construction of parametric model

In engineering design, parametric modeling refers to a modeling approach where dimensional attributes of a model are mathematically related to a reference geometry. Therefore, the change of the reference geometry transforms the size of the whole geometry maintaining a specific shape regulated by the pre-set parameter/dimensional relations. Considering that any biological system exhibits a great deal of variability in shape and size, we opted for the parametric modeling approach, which allowed us to develop a hair follicle model with generic shape based on dimensional data derived from the analysis of published images (Supplemental Table S1). The following are the principal steps of the construction of the parametric model.

Step 1 - Identification of a reference geometry: Considering that the ORS maintains a very consistent shape along the whole length of the hair follicle (red arrows in Supplementary Figure S1), it was chosen as the reference geometry.

Step 2 - Measurement of geometric dimensions with respect to the reference dimension, the radius of the ORS: Every dimension required to construct the hair follicle, such as length and width of dermal papilla, transition length, radius of IRS and cortex at different zones of the hair follicle (Supplementary Figure S1), were determined relative to the ORS radius.

Step 3 - Establishment of parametric relation: The average ($n=10$) of the ratio of each dimension with respect to the ORS was assigned as a parametric relation between that dimension and the reference. For example, the average length of the dermal papilla with respect to the ORS radius was found to be 1.28. Therefore, for a 140 μm ORS, the length of the DP was assigned as 180 μm .

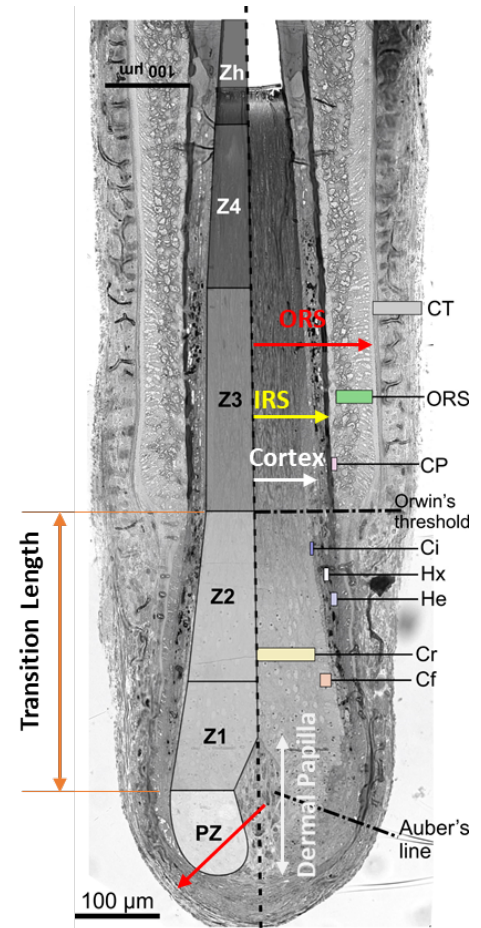


Figure S1: Parametric relationship development with respect to the reference ORS radius.